Geol. Mag. **155** (1), 2018, pp. 209–228. © Cambridge University Press 2017
doi:10.1017/S001675681700084X

RAPID COMMUNICATION

# *In situ* U–Th–$Pb_{total}$ dating of polychronous monazite in the Koraput anorthosite pluton, Eastern Ghats Granulite Belt (India), and implications

D. SAIKIA*, P. NASIPURI*†‡ & A. BHATTACHARYA§

*Department of Earth and Environmental Sciences, Indian Institute of Science Education and Research, Bhopal, India
‡Centre for Research on Environment and Sustainable Technologies, Indian Institute of Science Education and Research, Bhopal, India
§Department of Geology and Geophysics, Indian Institute of Technology Kharagpur, 721 302, India

(*Received* 20 February 2017; *accepted* 7 September 2017; *first published online* 30 October 2017)

## Abstract

U–Th–$Pb_{total}$ age determinations in monazite in a noritic anorthosite at the margin of the Koraput anorthosite pluton constrain the time of emplacement and sub-solidus chemical modifications in the Grenvillian-age anorthosite pluton in the Eastern Ghats Province (EGP), India. The monazites hosted within dynamically recrystallized orthopyroxene and plagioclase grains are large (50–500 μm in diameter) and complexly zoned. Based on the textural–chemical heterogeneities, these monazites are classified into three groups. Group-I monazites exhibit a low-$ThO_2$ core mantled by a high-$ThO_2$ rim. By contrast, the group-II monazites exhibit high-$ThO_2$ cores laced by $ThO_2$-poor mantles, and outermost rims with still lower $ThO_2$ contents. Skeletal group-III monazites at polygonized grain/phase boundaries exhibit patchy and concentric zones with decreasing $ThO_2$ towards the margin. The U–Th–$Pb_{total}$ chemical ages obtained using electron probe microanalyses exhibit four age clusters. The oldest age population (mean 939 ± 4.5 Ma) obtained in cores in group-I, II and III monazites with patchy zones corresponds with the emplacement of the Koraput anorthosite, and this age population is consistent with 980–930 Ma emplacement ages reported in other EGP anorthosite massifs. Younger monazites mantling the cores in group-II monazites and in group-III monazites with mean ages of 877 ± 5 Ma and 749 ± 18 Ma possibly reflect episodic monazite growth by fluid-aided dissolution–precipitation culminating with the disintegration of Rodinia at ~750 Ma. The youngest age population (mean 574 ± 19 Ma) in the outermost monazite rims and monazite veins represents renewed monazite growth during the Pan African assembly of the Grenvillian-age EGP domain with the proto-Indian cratons.

Keywords: polychronous monazite, U–Th–$Pb_{total}$ chemical age, Koraput anorthosite, Eastern Ghats Granulite Belt, Early Neoproterozoic–Pan African.

## 1. Introduction

Several unique features make monazite ((LREE)$PO_4$) ideally suited for dating multiple events in rocks that evolve over a wide range of metamorphic and magmatic conditions. Foremost among these features is the high closure temperature (≥750–800 °C) for Pb diffusion (Zhu *et al.* 1997; Zhu & O'Nions, 1999*a*,*b*; Cherniak *et al.* 2004; Gardés *et al.* 2006) in monazite that helps preserve magmatic and high-*T* metamorphic events in rocks. Second, monazite readily grows by fluid-aided dissolution and reprecipitation over a large range of temperatures, including temperatures prevailing at diagenetic conditions (Schärer *et al.* 1999; Rasmussen, Fletcher & Sheppard, 2005; Rasmussen & Muhling, 2007; Rekha, Bhattacharya & Viswanath, 2013), and therefore, monazite dating is a vital tool for constraining the age of low-*T* processes that may remain undetected by other dating techniques.

Radiometric dating of anorthosite is difficult because anorthosites lack minerals commonly used for age determinations, such as zircon, rutile and titanite. Zircon ($ZrSiO_4$) is unlikely to crystallize in anorthosite owing to the limited solubility of Zr in calc-alkaline magma (Watson & Harrison, 1983), although zircon is known to occur as xenocrysts entrained following crustal assimilation by anorthosite parent magma (Bhattacharya *et al.* 1998; Lackey, Hinke & Valley, 2002; Nasipuri, Bhattacharya & Satyanarayanan, 2011). On the other hand, rutile and titanite are lacking in anorthosite because with $TiO_2$ being a plagioclase-incompatible element, titanium saturation is rarely reached in anorthosite, although anorthosite residual melts are known to be enriched in $TiO_2$ (Bhattacharya *et al.* 1998 and references therein). Monazites are also rare in anorthosite (Parrish, 1990). Chatterjee *et al.* (2008) reported Neoproterozoic/Pan African monazites in a noritic anorthosite in Patharkata in the Balugaon anorthosite massif (Chilka Lake area; Fig. 1). In this study, we present the results of *in situ* chemical age determinations (Suzuki & Adachi, 1991*a*,*b*; Montel *et al.* 1996; Williams *et al.* 2006; Spear, Pyle & Cherniak, 2009) in polychronous monazites hosted within a noritic anorthosite in the Koraput massif close to the western margin of the Grenvillian-age granulites of the Eastern Ghats Province (Dobmeier & Raith, 2003) in the Eastern Ghats Granulite Belt (Fig. 1).

---

†Author for correspondence: pritams@iiserb.ac.in

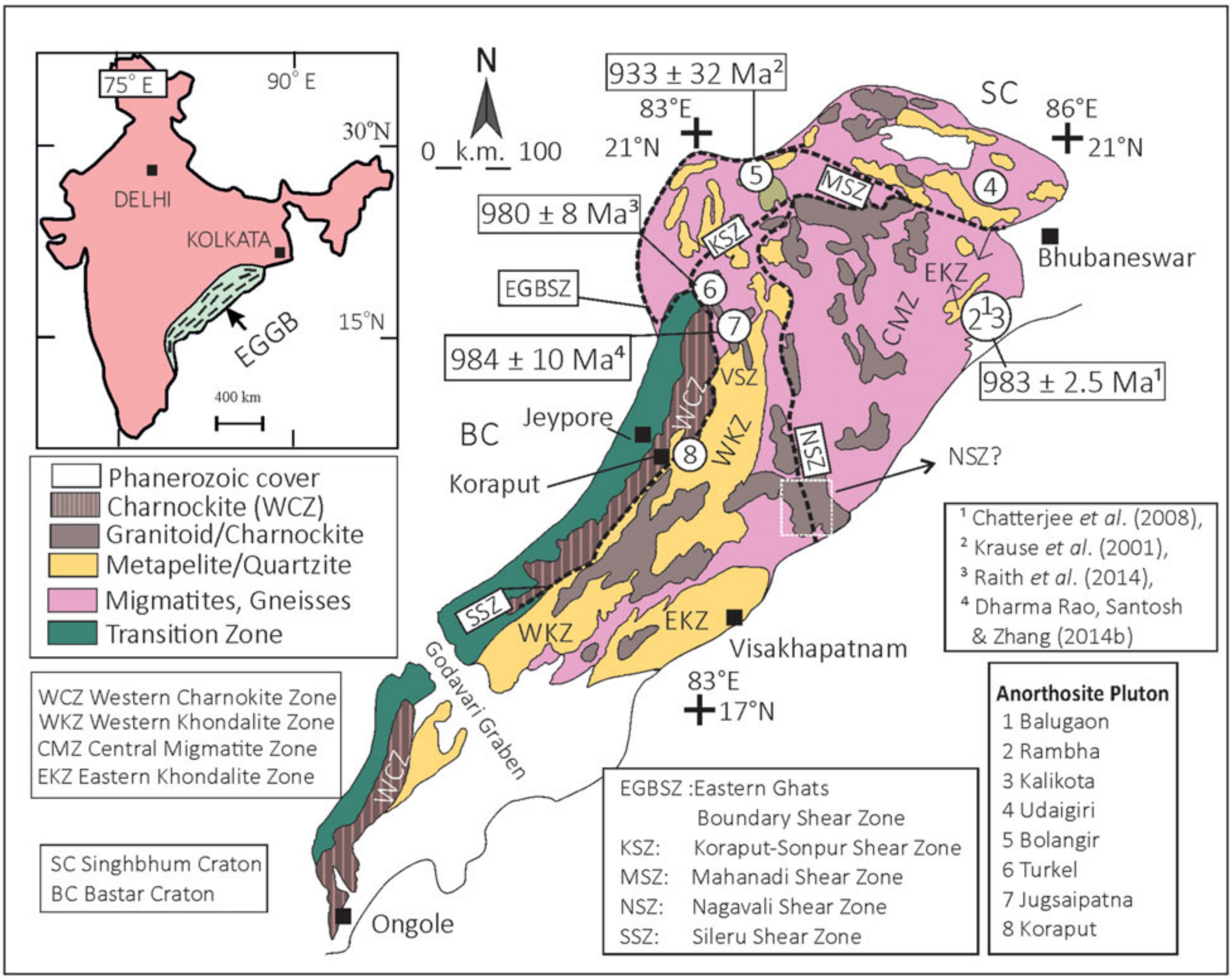

Figure 1. (Colour online) Lithodemic subdivisions of the Eastern Ghats Granulite Belt (EGGB; Ramakrishnan, Nanda & Augustine, 1998). The locations of anorthosite plutons are shown with filled circles, and the inferred emplacement ages are indicated in boxes (Leelanandam & Reddy, 1988; Nanda & Panda, 1999). The references to the emplacement age are keyed as superscripts against the age data. Kalikot, Balugaon and Rambha are parts of the Chilka Lake anorthosite massif. Shear zones demarcating boundaries of 'provinces' are after Chetty & Murthy (1994).

## 2. Geological background

Ramakrishnan, Nanda & Augustine (1998) sub-divided the Eastern Ghats Granulite Belt (EGGB) into four lithodemic units, e.g. the Western Charnockite Zone (WCZ), the Western Khondalite (garnet–sillimanite–K-feldspar–quartz) Zone (WKZ), the Central Migmatite Zone (CMZ) and the Eastern Khondalite Zone (EKZ) (Fig. 1). Rickers, Mezger & Raith (2001) sub-divided the EGGB into different isotopic domains. Integrating the Nd isotopic character with the deformation history and metamorphism, Dobmeier & Raith (2003) suggested the EGGB was a mosaic of accreted 'domains' and 'provinces' each having distinct tectonothermal histories. The youngest of the provinces, the Eastern Ghats Province (EGP), comprising isotopic Domains 2 and 3 of Rickers, Mezger & Raith (2001), is exposed in the north-central and south-central parts of the EGGB (Fig. 1).

The boundaries separating the provinces and the interface between the provinces at the EGGB margin and the Archaean cratons of Bastar in the west and Singhbhum in the north are delineated by regional-scale ductile shear zones (Chetty & Murthy, 1994, Fig. 1). The NNE-trending Sileru Shear Zone (SSZ) (Dobmeier & Raith, 2003) demarcates the boundary between the WKZ and the WCZ of Ramakrishnan, Nanda & Augustine (1998). A series of alkaline plutons and anorthosite massifs (Fig. 1) occur in the neighbourhood of the SSZ (Dobmeier & Raith, 2003).

The high-grade gneisses, barring those in the WCZ, experienced Grenvillian-age (Rickers, Mezger & Raith, 2001) high-*T* counter-clockwise *P*–*T* paths (Bose *et al.* 2011 and references therein; Korhonen *et al.* 2011, 2013). The similarity in metamorphic conditions in the EGP granulites (Bose *et al.* 2011) and the Rayner Complex, Eastern Antarctica (Harley, Fitzsimons & Zhao, 2013) led several researchers to suggest the terrain boundary shear zone to be the zone of accretion between the Bastar craton vis-à-vis the cratonic nucleus of India and the EGP–Rayner Complex composite (Chetty & Murthy, 1994; Gupta *et al.* 2000; Dobmeier & Raith, 2003; Bhattacharya *et al.* 2016). However, the time of accretion of the EGP with the craton is debated (Black *et al.* 1987; Shaw *et al.* 1997; Mezger & Cosca, 1999; Halpin *et al.* 2005; Das *et al.* 2008; Harley, Fitzsimons & Zhao, 2013). Based on the palaeogeographic reconstruction for India, Eastern Antarctica and Australia, Torsvik (2013) argued that the Bastar craton–EGP–Eastern Antarctica accretion to be Pan African in age. A Pan African accretion of the EGP with the Bastar craton during the final assembly of Gondwanaland has been suggested by Biswal, De Waele & Ahuja (2007) and

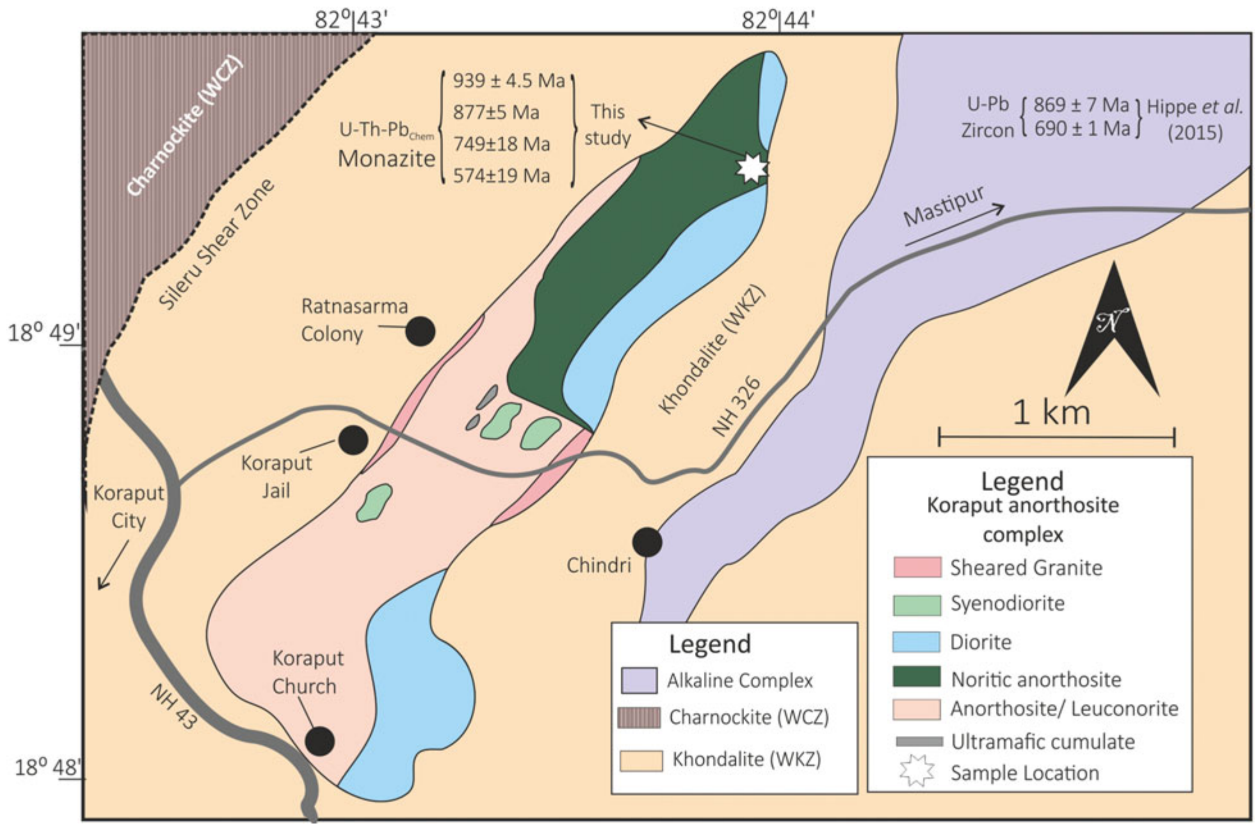

Figure 2. (Colour online) Geological map showing the Koraput anorthosite complex (modified after Bose, 1960), the southern part of the Koraput alkaline complex (Hippe *et al.* 2015) and the trace of the Sileru Shear Zone (Chetty & Murthy, 1994). The location of the monazite-bearing sample within the Koraput anorthosite complex is marked by a filled star. Chronological information for the Koraput alkaline complex (Hippe *et al.* 2015) and Koraput anorthosite complex (this study) are provided for comparison.

Das *et al.* (2008), more recently by Bhattacharya *et al.* (2016) and subsequently by Chatterjee *et al.* (2017). Another phase of mid-Neoproterozoic (800–750 Ma) high-grade metamorphism is being increasingly recognized in the EGP granulites, albeit in localized zones in and neighbouring the Mahanadi Shear Zone (Veevers, 2007; Veevers & Saeed, 2009; Bhattacharya *et al.* 2016) and near the Chilka Lake Complex (Bose *et al.* 2016) along the northern margin of the EGGB. This mid-Neoproterozoic (800–750 Ma) event is correlated with a phase of extensional tectonics related to the eventual break-up of Rodinia (Torsvik, 2003).

In the Grenvillian-age EGP comprising the WKZ, CMZ and EKZ, massif anorthosites occur at Chilka Lake (Sarkar, Bhanumathi & Balasubrahmanyan, 1981; Bhattacharya, Sen & Acharyya, 1994; Mukherjee, Jana & Das, 1999; Krause *et al.* 2001; Dobmeier & Simmat, 2002; Chatterjee *et al.* 2008), Bolangir (Tak, Mitra & Chatterjee, 1966; Tak, 1971; Mukherjee, Bhattacharya & Chakravorty, 1986; Raith, Bhattacharya & Hoernes, 1997; Bhattacharya *et al.* 1998; Mukherjee, Jana & Das, 1999; Krause *et al.* 2001; Prasad *et al.* 2005; Nasipuri & Bhattacharya, 2007; Nasipuri, Bhattacharya & Satyanarayanan, 2011; Nasipuri & Bhadra, 2013), Turkel (Maji, Bhattacharya & Raith, 1997; Maji & Sarkar, 2004; Raith *et al.* 2014; Dharma Rao, Santosh & Zhang, 2014*a*), Jugsaipatna (Mahapatro, Nanda & Tripathy, 2010; Dharma Rao, Santosh & Zhang, 2014*b*), Koraput (Bose, 1960, 1979) and Udaigiri (Mahapatro *et al.* 2013). The central parts of the plutons are dominated by anorthosite, whereas leuconorite and noritic anorthosite dominate the pluton margins. Pods of ultramafic cumulate and veins of high-alumina-gabbro are reported in the Bolangir pluton (Bhattacharya *et al.* 1998) and the Koraput anorthosite complex (Bose, 1960). The plutons are bordered by blastoporphyritic granitoids that are mangerite, charnockite and granite in composition. Fe-rich, Si-poor ferrodiorite (also referred to as ferrojotunite) enriched in plagioclase-incompatible high-field strength elements such as Zr, Ti, Th, P and rare earth elements (REEs) occurs as sheets and veins neighbouring or at the pluton–granitoid interface (Bose, 1960; Maji, Bhattacharya & Raith, 1997; Bhattacharya *et al.* 1998; Chatterjee *et al.* 2008; Nasipuri, Bhattacharya & Satyanarayanan, 2011). Along the margin of the pluton, the low-K anorthosite–ferrodiorite and high-K mangerite–charnockite–granite suites are characterized by a prominent margin-parallel foliation defined by biotite and dynamically recrystallized orthopyroxene that weakens radially from the pluton margin (Nasipuri & Bhattacharya, 2007).

Barring the 1387 Ma age for the Chilka Lake pluton obtained using whole-rock $^{87}$Rb–$^{87}$Sr in anorthosite and bordering granitoids (Sarkar, Bhanumathi & Balasubrahmanyan, 1981), more recent age determinations in the EGP anorthosites are based on U–Pb and Pb–Pb radiogenic isotope systematic and chemical U–Th–Pb$_{total}$ dating in zircons and monazites in high-K granitoids (bordering anorthosite plutons) that are assumed contemporaneous with the low-K anorthosite–leuconorite suite, and also in ferrodiorites deemed to be co-magmatic with the anorthosite suite (Bhattacharya *et al.* 1998). Krause *et al.* (2001) determined an age of 792 ± 2 Ma from U–Pb

Figure 3. (Colour online) Field photographs of the Koraput anorthosite complex. (a) Bimodal grain size population among plagioclase in the Koraput anorthosite, e.g. relics of grey-coloured magmatic plagioclase (outlined by a white line) embedded in a finer-grained sugary mosaic of recrystallized plagioclase. (b) Lack of penetrative planar fabric in leuconorite in the pluton interior. (c, d) Biotite aggregates defining margin-parallel foliation (M–M′) in noritic anorthosite. Coin diameter is 2.3 cm. Length of hammer is 40 cm.

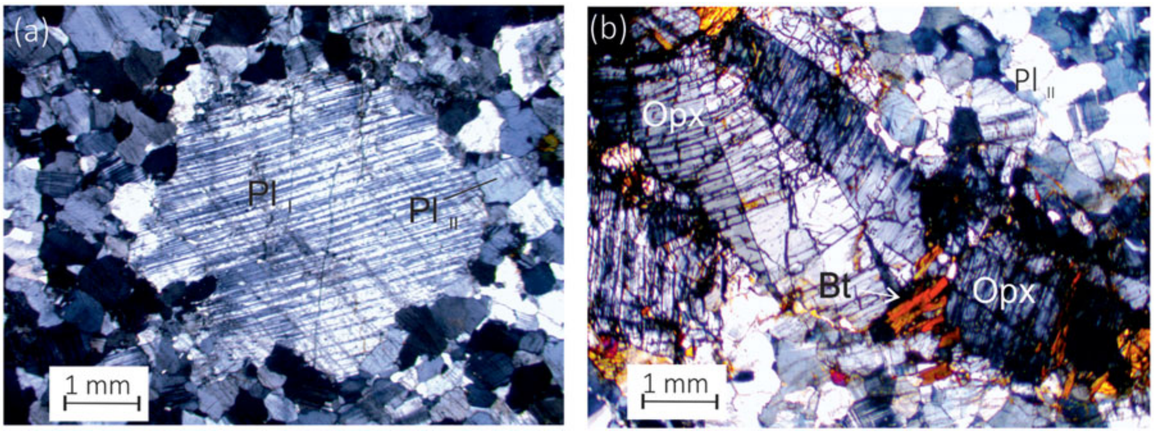

Figure 4. (Colour online) Microphotographs of (a) relics of igneous feldspar in a matrix of finer-grained aggregates of polygonized plagioclase showing undulatory extinction, and (b) undulose extinction and sub-grain formation in magmatic orthopyroxene grains ($X_{Mg} = 0.50$). Biotite is replacing orthopyroxene along the periphery in (b).

(zircon) in ferrodiorite in the Balugaon massif. Chatterjee *et al.* (2008) estimated the crystallization age (U–Pb zircon) in noritic anorthosite from the Balugaon pluton in the Chilka Lake Complex to be 983 ± 3 Ma; the U–Th–Pb chemical ages in monazites yielded two age populations at 714 ± 11 Ma and 655 ± 12 Ma. In the Bolangir pluton, U–Pb zircon isotope ratios in ferrodiorite are discordant, with a U–Pb upper intercept age at 933 ± 32 Ma, and a lower intercept age of 515 ± 20 Ma (Krause *et al.* 2001) coinciding with near-concordant U–Pb titanite in calc-silicate rocks at the pluton margin (Mezger & Cosca, 1999). Based on U–Pb analysis of zircon from different magmatic units in the Turkel anorthosite complex, Raith *et al.* (2014) suggested the leuconorite–anorthosite unit at Turkel was emplaced at 980 ± 8 Ma followed by the crystallization of quartz monzonite and ferrodiorite at 956 ± 6 Ma and 945 ± 5 Ma. Pb–Pb zircon ages in the Jugsaipatna anorthosite complex yielded crystallization ages between 918 ± 33 Ma and 928 ± 35 Ma for two leuconorite samples, 984 ± 10 Ma and 969 ± 12 Ma for gabbros

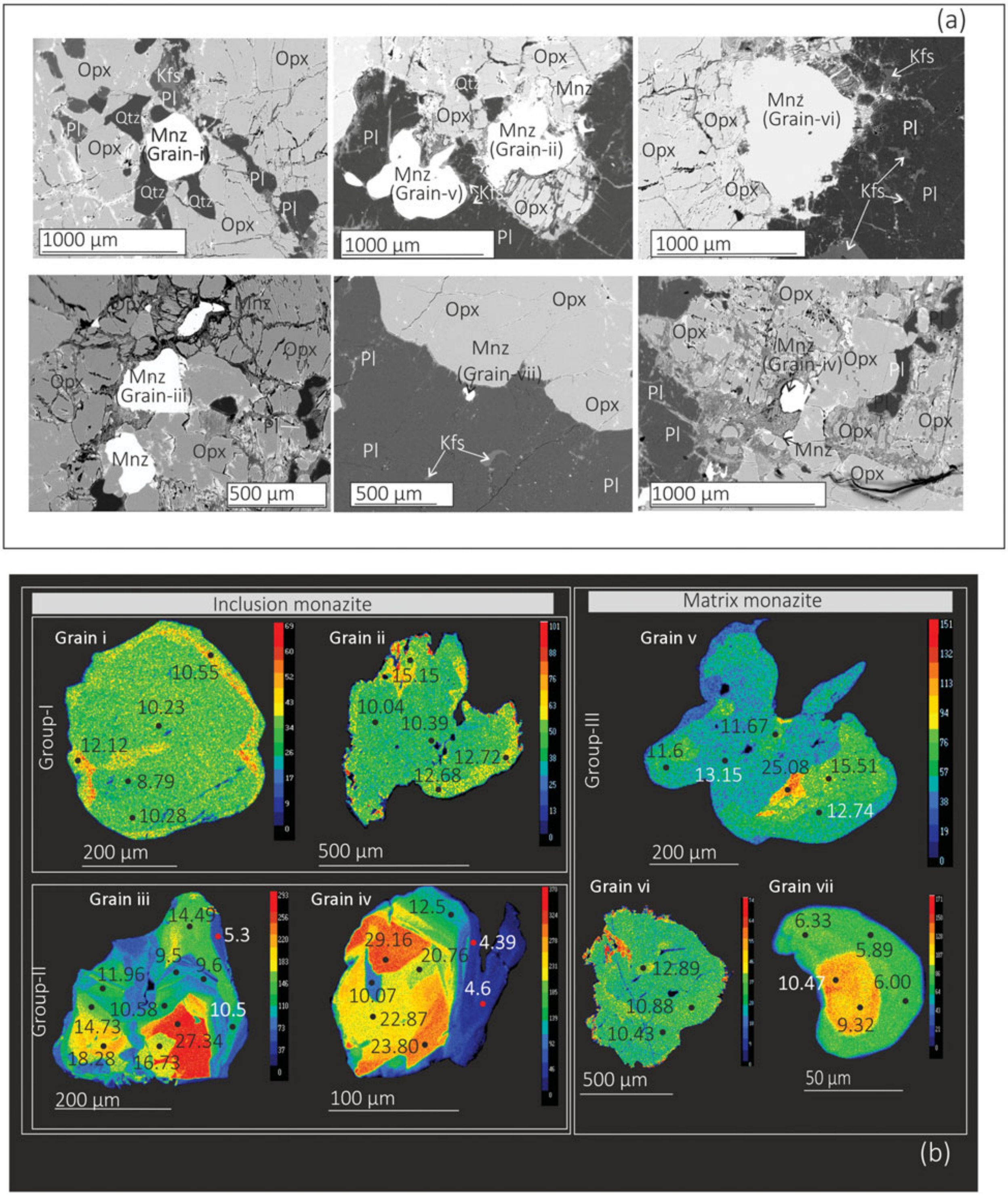

Figure 5 (Colour online) (a) BSE images showing textural settings of monazite-dated grains and (b) $ThO_2$ X-ray element maps. The analysed $ThO_2$ contents in weight per cent are shown for reference.

bordering the pluton, and 996 ± 11 Ma, 964 ± 29 Ma and 957 ± 17 Ma for porphyritic granites (Dharma Rao, Santosh & Zhang, 2014*b*). The data suggest anorthosite magmatism and high-*T* metamorphism in the EGP was broadly contemporaneous.

## 3. The Koraput anorthosite pluton

The NNE-trending anorthosite pluton at Koraput, Orissa (Bose, 1960; Fig. 2) hosted within the WKZ (garnet-sillimanite gneisses) is the smallest (long axis is 3 km) among the anorthosite plutons in the EGP. Owing to extensive soil cover and human settlements, the pluton is now poorly exposed. An examination of scattered outcrops E/NE of Koraput suggests the complex is dominated by anorthosite *sensu stricto*, with noritic anorthosite, and diorite/ferrodiorite common along the eastern margin. The anorthosite/noritic anorthosite exhibits bimodal grain-size populations with anhedral grey-coloured magmatic plagioclase grains (up to 2 cm long) embedded in a sugary-white mosaic of finer-grained polygonized plagioclase (Fig. 3a). Both the magmatic and the

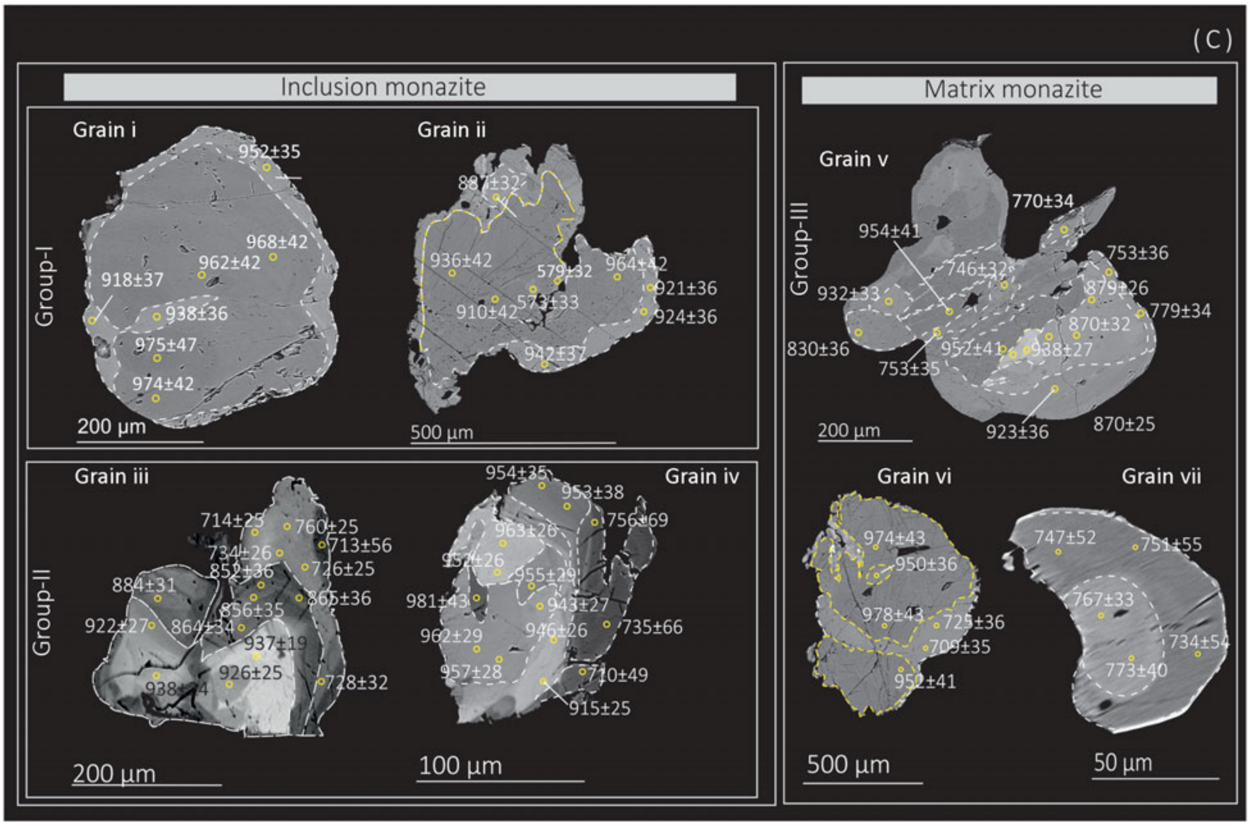

Figure 5 (Continued) (Colour online). (c) BSE images of monazite grains. Monazite spot ages are shown. In the monazite grains i and ii, the cores have low $ThO_2$ contents, while the brighter margins have higher $ThO_2$ contents. Monazite grains iii and iv with bright $ThO_2$-rich cores are mantled by progressively $ThO_2$-poorer mantles. Concentric zoning is preserved in the high-$ThO_2$ core and in the intermediate-$ThO_2$ mantle (grain iii). Monazite grains in the matrix exhibit patchy (v, vi) and concentric zoning (vii).

polygonized plagioclases are andesine in composition (38–42 mol. % anorthite), and exhibit strain wavy extinction and cuspate-lobate grain boundaries (Fig. 4a). Dynamically recrystallized orthopyroxene grains typically 2–3 mm long display undulatory extinction and kink bands (Fig. 4b). Relics of magmatic plagioclase grains are fewer and smaller in the east, and intergranular textures, common in the west (Fig. 3b), are strongly deformed towards the east. The eastward increase in deformation strain is consistent with the development of an outward-dipping penetrative tectonic fabric mostly defined by biotite (Fig. 3c, d). The biotite aggregates partially replace dynamically recrystallized orthopyroxene (Fig. 4b), and also occur as discrete grains in the polygonized mosaic of plagioclase.

## 4. Mineral chemistry of monazite

Monazite grains were analysed using a CAMECA SX-100 Electron Probe Micro Analyser (EPMA) at the Department of Geology and Geophysics, Indian Institute of Technology Kharagpur, India. The analytical protocols and data reduction techniques are adopted from Prabhakar (2013), and only a brief outline is provided here. During analysis, the accelerating voltage was 20 kV, beam current 150 nA, and beam size was 1.0 µm diameter. The following standards were used: galena for Pb, $UO_2$ for U, $ThO_2$ for Th, synthetic silica-aluminium glass containing 4 % REEs for La, Ce, Nd, Pr, Sm, Ho, Dy and Gd, and apatite for P and Ca; yttrium-aluminium garnet (YAG) was used for Y, corundum for Al, haematite for Fe and Th-glass for Si (silica). Counting time for Th (Mα), U (Mβ) and Pb (Mα) was set between 200 and 300 seconds, and 40–60 seconds for REEs. The spectral interferences of Th on U and Y on Pb were corrected using the inbuilt analytical software of the Cameca SX-100. The chemical composition of the spot analysis was translated to spot age by the expression following Montel *et al.* (1996):

$$Pb = \frac{Th}{232}[e^{\lambda 232t} - 1]208 + \frac{U}{238}0.9928[e^{\lambda 238t} - 1]206 + \frac{U}{235}0.0072[e^{\lambda 235t} - 1]207 \qquad (1)$$

The U, Th and Pb concentrations are in parts per million (ppm), $t$ represents age in years and $\lambda^{238}$ and $\lambda^{235}$ are decay constants for $Th^{232}$ ($4.95 \times 10^{-11}$ $year^{-1}$), $U^{238}$ ($1.55 \times 10^{-10}$ $year^{-1}$) and $U^{235}$ ($9.85 \times 10^{-10}$ $year^{-1}$) (Steiger & Jäger, 1977). The equation is solved iteratively to obtain the spot ages. The Moacyr monazite standard was analysed simultaneously to control the consistency of the spot analysis (Prabhakar, 2013).

Monazite occurs as inclusions within dynamically recrystallized orthopyroxene and as discrete grains within the polygonized plagioclase matrix (Fig. 5a). $ThO_2$ contents in the Koraput monazites vary between 4.4 and 30.8 wt % for all grains taken together (Fig. 5; Table 1). Based on the shades in the BSE (back-scattered electron) images, orthopyroxene-hosted monazite grains are divided into two broad groups (Fig. 5b, c). In group-I grains (diameter up to 500 µm), the $ThO_2$-poor (8.79–10.28 wt %) dark core is mantled by a 10–20 µm wide $ThO_2$-rich (9.71–14.28 wt %) bright rim (grains i, ii in Fig. 5b, c) resembling normal zones in concentrically zoned monazites (c.f. Zhu & O'Nions, 1999*b*; Majka *et al.* 2012). The group-II

Table 1. Electron probe microanalytical data, structural formulae (based on 4 oxygens per formula unit), spot ages and 2σ errors (in Ma), error % (= 100 (error)/(absolute age)) and mole fractions of La–Ce–Nd monazite, cheralite and huttonite end-members in monazites in the Koraput noritic anorthosite

| | Group-I monazite | | | | | | | | | | | | | | | | | |
|---|---|---|---|---|---|---|---|---|---|---|---|---|---|---|---|---|---|---|
| | Grain i | | | | | | | | Grain ii | | | | | | | | | |
| | rim | rim | rim | core | core | core | core | | rim | rim | rim | rim | rim | rim | rim | rim | core | core |
| $P_2O_5$ | 27.40 | 27.80 | 27.46 | 29.30 | 29.81 | 28.57 | 28.70 | $P_2O_5$ | 27.05 | 27.15 | 27.12 | 27.70 | 27.43 | 27.31 | 27.50 | 26.99 | 29.22 | 29.10 |
| $SiO_2$ | 2.21 | 2.15 | 2.11 | 0.99 | 0.75 | 1.32 | 1.33 | $SiO_2$ | 2.14 | 2.26 | 2.29 | 2.12 | 2.19 | 2.18 | 2.18 | 2.41 | 1.15 | 1.17 |
| $ThO_2$ | 13.20 | 12.12 | 13.55 | 10.30 | 8.80 | 10.23 | 10.40 | $ThO_2$ | 10.39 | 11.01 | 10.84 | 12.38 | 12.75 | 12.72 | 12.68 | 15.15 | 10.31 | 10.04 |
| $UO_2$ | 0.12 | 0.12 | 0.12 | 0.12 | 0.14 | 0.10 | 0.10 | $UO_2$ | 0.09 | 0.10 | 0.10 | 0.12 | 0.10 | 0.10 | 0.12 | 0.11 | 0.12 | 0.10 |
| $Al_2O_3$ | 0.04 | 0.03 | 0.05 | 0.04 | 0.03 | 0.03 | 0.04 | $Al_2O_3$ | 0.04 | 0.04 | 0.04 | 0.05 | 0.04 | 0.05 | 0.05 | 0.05 | 0.04 | 0.02 |
| $Y_2O_3$ | 0.06 | 0.15 | 0.09 | 0.27 | 0.30 | 0.29 | 0.24 | $Y_2O_3$ | 0.15 | 0.14 | 0.11 | 0.10 | 0.09 | 0.07 | 0.08 | 0.09 | 0.18 | 0.12 |
| $La_2O_3$ | 13.90 | 13.80 | 13.32 | 13.80 | 14.23 | 14.46 | 14.60 | $La_2O_3$ | 13.93 | 14.02 | 14.20 | 14.19 | 14.14 | 14.33 | 14.25 | 13.71 | 13.73 | 14.09 |
| $Ce_2O_3$ | 27.70 | 28.09 | 27.26 | 27.50 | 27.89 | 27.56 | 27.60 | $Ce_2O_3$ | 27.99 | 28.26 | 28.10 | 27.72 | 27.61 | 27.46 | 27.55 | 26.13 | 27.69 | 27.92 |
| $Pr_2O_3$ | 2.78 | 2.97 | 2.79 | 2.82 | 2.85 | 2.82 | 2.85 | $Pr_2O_3$ | 2.91 | 2.89 | 2.88 | 2.83 | 2.77 | 2.80 | 2.73 | 2.52 | 2.92 | 2.89 |
| $Nd_2O_3$ | 10.30 | 10.69 | 10.06 | 10.60 | 10.46 | 10.27 | 10.30 | $Nd_2O_3$ | 11.40 | 11.55 | 11.42 | 10.62 | 10.50 | 10.24 | 10.41 | 9.89 | 11.36 | 11.25 |
| $Gd_2O_3$ | 0.46 | 0.61 | 0.43 | 0.79 | 0.87 | 0.72 | 0.58 | $Gd_2O_3$ | 0.64 | 0.54 | 0.48 | 0.51 | 0.43 | 0.43 | 0.42 | 0.44 | 0.64 | 0.51 |
| $Dy_2O_3$ | 0.09 | 0.10 | 0.08 | 0.12 | 0.18 | 0.12 | 0.14 | $Dy_2O_3$ | 0.03 | 0.05 | 0.07 | 0.04 | 0.07 | 0.06 | 0.07 | 0.07 | 0.05 | 0.05 |
| $Sm_2O_3$ | 1.20 | 1.35 | 1.18 | 1.46 | 1.58 | 1.32 | 1.28 | $Sm_2O_3$ | 1.29 | 1.29 | 1.26 | 1.06 | 1.06 | 1.09 | 0.99 | 1.08 | 1.37 | 1.29 |
| $Eu_2O_3$ | 0.06 | 0.11 | 0.10 | 0.09 | 0.05 | 0.07 | 0.06 | $Eu_2O_3$ | 0.13 | 0.06 | 0.10 | 0.00 | 0.03 | 0.05 | 0.08 | 0.07 | 0.07 | 0.15 |
| CaO | 1.10 | 0.90 | 1.26 | 1.59 | 1.55 | 1.30 | 1.32 | CaO | 0.52 | 0.62 | 0.64 | 1.01 | 1.02 | 1.03 | 1.03 | 1.31 | 1.47 | 1.38 |
| PbO | 0.55 | 0.49 | 0.57 | 0.45 | 0.39 | 0.44 | 0.45 | PbO | 0.26 | 0.28 | 0.28 | 0.48 | 0.52 | 0.52 | 0.53 | 0.59 | 0.44 | 0.42 |
| Total | 101.0 | 101.4 | 100.0 | 100.0 | 99.8 | 99.6 | 100.0 | Total | 98.89 | 100.18 | 99.87 | 100.85 | 100.70 | 100.38 | 100.60 | 100.50 | 100.70 | 100.40 |
| **Age** (Ma) | 938 | 918 | 952 | 974 | 975 | 962 | 968 | **Age** (Ma) | 573 | 571 | 579 | 869 | 921 | 924 | 942 | 887 | 964 | 936 |
| $2\sigma$ err | 36 | 37 | 35 | 42 | 47 | 42 | 42 | $2\sigma$ err | 33 | 32 | 32 | 36 | 36 | 36 | 37 | 32 | 42 | 42 |
| Error% | 3.84 | 4.03 | 3.68 | 4.31 | 4.82 | 4.37 | 4.34 | Error% | 5.76 | 5.60 | 5.53 | 4.14 | 3.91 | 3.90 | 3.93 | 3.61 | 4.36 | 4.49 |
| | | | | | | | | | Cations | | | | | | | | | |
| P | 0.901 | 0.906 | 0.906 | 0.951 | 0.964 | 0.938 | 0.938 | P | 0.905 | 0.899 | 0.899 | 0.908 | 0.904 | 0.903 | 0.906 | 0.896 | 0.945 | 0.945 |
| Si | 0.086 | 0.083 | 0.082 | 0.038 | 0.029 | 0.051 | 0.051 | Si | 0.084 | 0.088 | 0.089 | 0.082 | 0.085 | 0.085 | 0.085 | 0.094 | 0.044 | 0.045 |
| Th | 0.116 | 0.106 | 0.120 | 0.090 | 0.076 | 0.090 | 0.092 | Th | 0.093 | 0.098 | 0.097 | 0.109 | 0.113 | 0.113 | 0.112 | 0.135 | 0.090 | 0.088 |
| U | 0.001 | 0.001 | 0.001 | 0.001 | 0.001 | 0.001 | 0.001 | U | 0.001 | 0.001 | 0.001 | 0.001 | 0.001 | 0.001 | 0.001 | 0.001 | 0.001 | 0.001 |
| Al | 0.002 | 0.002 | 0.002 | 0.002 | 0.001 | 0.001 | 0.002 | Al | 0.002 | 0.002 | 0.002 | 0.002 | 0.002 | 0.002 | 0.002 | 0.002 | 0.002 | 0.001 |
| Y | 0.001 | 0.003 | 0.002 | 0.005 | 0.006 | 0.006 | 0.005 | Y | 0.003 | 0.003 | 0.002 | 0.002 | 0.002 | 0.001 | 0.002 | 0.002 | 0.004 | 0.002 |
| La | 0.200 | 0.196 | 0.192 | 0.195 | 0.200 | 0.207 | 0.208 | La | 0.203 | 0.202 | 0.205 | 0.203 | 0.203 | 0.206 | 0.204 | 0.198 | 0.193 | 0.199 |
| Ce | 0.393 | 0.396 | 0.389 | 0.387 | 0.390 | 0.391 | 0.390 | Ce | 0.405 | 0.405 | 0.403 | 0.393 | 0.393 | 0.392 | 0.392 | 0.375 | 0.387 | 0.392 |
| Pr | 0.097 | 0.102 | 0.098 | 0.097 | 0.098 | 0.098 | 0.098 | Pr | 0.103 | 0.101 | 0.101 | 0.098 | 0.096 | 0.098 | 0.095 | 0.089 | 0.100 | 0.099 |
| Nd | 0.143 | 0.147 | 0.140 | 0.145 | 0.143 | 0.142 | 0.142 | Nd | 0.161 | 0.161 | 0.160 | 0.147 | 0.146 | 0.143 | 0.145 | 0.138 | 0.155 | 0.154 |
| Gd | 0.006 | 0.008 | 0.006 | 0.010 | 0.011 | 0.009 | 0.007 | Gd | 0.008 | 0.007 | 0.006 | 0.007 | 0.006 | 0.006 | 0.005 | 0.006 | 0.008 | 0.006 |
| Dy | 0.001 | 0.001 | 0.001 | 0.001 | 0.002 | 0.001 | 0.002 | Dy | 0.000 | 0.001 | 0.001 | 0.001 | 0.001 | 0.001 | 0.001 | 0.001 | 0.001 | 0.001 |
| Sm | 0.016 | 0.018 | 0.016 | 0.019 | 0.021 | 0.018 | 0.017 | Sm | 0.018 | 0.017 | 0.017 | 0.014 | 0.014 | 0.015 | 0.013 | 0.015 | 0.018 | 0.017 |
| Eu | 0.001 | 0.001 | 0.001 | 0.001 | 0.001 | 0.001 | 0.001 | Eu | 0.002 | 0.001 | 0.001 | 0.000 | 0.000 | 0.001 | 0.001 | 0.001 | 0.001 | 0.002 |
| Ca | 0.046 | 0.037 | 0.052 | 0.065 | 0.063 | 0.054 | 0.055 | Ca | 0.022 | 0.026 | 0.027 | 0.042 | 0.043 | 0.043 | 0.043 | 0.055 | 0.060 | 0.057 |
| Pb | 0.006 | 0.005 | 0.006 | 0.005 | 0.004 | 0.005 | 0.005 | Pb | 0.003 | 0.003 | 0.003 | 0.005 | 0.005 | 0.005 | 0.006 | 0.006 | 0.005 | 0.004 |
| Total | 2.015 | 2.013 | 2.014 | 2.013 | 2.011 | 2.014 | 2.013 | Total | 2.012 | 2.015 | 2.015 | 2.013 | 2.014 | 2.015 | 2.013 | 2.013 | 2.013 | 2.013 |
| $X_{\text{Hutt.}}$ | 0.075 | 0.074 | 0.073 | 0.029 | 0.018 | 0.041 | 0.042 | $X_{\text{Hutt.}}$ | 0.073 | 0.074 | 0.072 | 0.072 | 0.075 | 0.074 | 0.074 | 0.086 | 0.034 | 0.035 |
| $X_{\text{Cher.}}$ | 0.089 | 0.072 | 0.103 | 0.128 | 0.125 | 0.106 | 0.107 | $X_{\text{Cher.}}$ | 0.043 | 0.051 | 0.052 | 0.082 | 0.083 | 0.084 | 0.084 | 0.107 | 0.118 | 0.111 |
| $X_{\text{Mon.}}$ | 0.836 | 0.854 | 0.824 | 0.843 | 0.857 | 0.854 | 0.852 | $X_{\text{Mon.}}$ | 0.884 | 0.875 | 0.876 | 0.846 | 0.842 | 0.841 | 0.841 | 0.807 | 0.848 | 0.854 |

Table 1. Continued

| Group-II monazite | | | | | | | | | | | | | | | | | |
|---|---|---|---|---|---|---|---|---|---|---|---|---|---|---|---|---|---|
| Grain iii | | | | | | | | | | | | | | | | | |
| | core | core | core | core | rim | rim | rim | rim | rim | rim | rim | rim | rim | rim | rim | rim | rim |
| $P_2O_5$ | 22.20 | 25.46 | 24.78 | 26.02 | 26.52 | 28.41 | 27.93 | 28.20 | 25.97 | 26.93 | 26.61 | 26.51 | 27.98 | 27.53 | 28.10 | 27.28 | 29.31 |
| $SiO_2$ | 5.02 | 2.98 | 3.31 | 2.56 | 2.65 | 1.58 | 1.72 | 1.36 | 1.90 | 2.54 | 2.50 | 2.61 | 1.63 | 1.84 | 1.70 | 2.11 | 0.99 |
| $ThO_2$ | 27.34 | 16.73 | 18.28 | 14.73 | 14.49 | 9.50 | 10.07 | 7.35 | 10.50 | 14.36 | 13.58 | 14.17 | 9.62 | 10.58 | 10.09 | 11.96 | 5.25 |
| $UO_2$ | 0.14 | 0.12 | 0.13 | 0.13 | 0.12 | 0.11 | 0.12 | 0.09 | 0.10 | 0.14 | 0.11 | 0.14 | 0.10 | 0.12 | 0.10 | 0.10 | 0.07 |
| $Al_2O_3$ | 0.09 | 0.06 | 0.06 | 0.05 | 0.05 | 0.03 | 0.05 | 0.02 | 0.04 | 0.05 | 0.03 | 0.04 | 0.04 | 0.03 | 0.04 | 0.03 | 0.01 |
| $Y_2O_3$ | 0.08 | 0.07 | 0.08 | 0.06 | 0.15 | 0.09 | 0.12 | 0.15 | 0.14 | 0.16 | 0.16 | 0.16 | 0.08 | 0.08 | 0.08 | 0.09 | 0.17 |
| $La_2O_3$ | 10.81 | 13.51 | 12.98 | 13.82 | 12.63 | 14.34 | 14.63 | 14.81 | 14.41 | 12.45 | 12.60 | 12.33 | 14.19 | 14.17 | 13.98 | 13.41 | 14.79 |
| $Ce_2O_3$ | 20.65 | 25.63 | 24.86 | 26.73 | 26.45 | 29.17 | 28.84 | 30.00 | 28.39 | 25.30 | 25.92 | 25.69 | 28.08 | 27.40 | 27.55 | 26.90 | 30.83 |
| $Pr_2O_3$ | 2.16 | 2.66 | 2.53 | 2.76 | 2.79 | 3.00 | 2.98 | 3.14 | 2.92 | 2.90 | 2.90 | 2.90 | 3.07 | 2.88 | 2.97 | 2.92 | 3.26 |
| $Nd_2O_3$ | 7.34 | 8.80 | 8.58 | 9.23 | 10.41 | 10.50 | 10.10 | 11.21 | 10.36 | 9.96 | 10.34 | 10.46 | 10.14 | 9.80 | 10.31 | 9.89 | 11.90 |
| $Gd_2O_3$ | 0.48 | 0.49 | 0.43 | 0.51 | 0.67 | 0.58 | 0.66 | 0.66 | 0.60 | 0.70 | 0.67 | 0.71 | 0.61 | 0.49 | 0.60 | 0.61 | 0.73 |
| $Dy_2O_3$ | 0.12 | 0.06 | 0.10 | 0.02 | 0.09 | 0.05 | 0.07 | 0.10 | 0.09 | 0.08 | 0.08 | 0.08 | 0.04 | 0.05 | 0.05 | 0.06 | 0.09 |
| $Sm_2O_3$ | 0.96 | 1.08 | 1.03 | 1.15 | 1.49 | 1.43 | 1.31 | 1.53 | 1.33 | 1.43 | 1.51 | 1.45 | 1.32 | 1.26 | 1.34 | 1.33 | 1.69 |
| $Eu_2O_3$ | 0.00 | 0.00 | 0.00 | 0.00 | 0.11 | 0.04 | 0.00 | 0.07 | 0.00 | 0.01 | 0.06 | 0.11 | 0.02 | 0.00 | 0.05 | 0.05 | 0.11 |
| CaO | 1.47 | 1.09 | 1.12 | 0.99 | 0.90 | 0.76 | 0.79 | 0.53 | 0.76 | 0.87 | 0.84 | 0.86 | 0.79 | 0.80 | 0.79 | 0.84 | 0.48 |
| PbO | 1.12 | 0.68 | 0.76 | 0.60 | 0.48 | 0.36 | 0.40 | 0.24 | 0.34 | 0.45 | 0.44 | 0.45 | 0.37 | 0.41 | 0.38 | 0.47 | 0.17 |
| Total | 99.92 | 99.36 | 98.98 | 99.29 | 99.92 | 99.88 | 99.71 | 99.39 | 97.76 | 98.26 | 98.26 | 98.61 | 97.99 | 97.35 | 98.07 | 97.97 | 99.76 |
| Age (Ma) | 937 | 926 | 938 | 922 | 760 | 852 | 892 | 718 | 728 | 714 | 734 | 726 | 865 | 864 | 856 | 884 | 713 |
| Age err | 19 | 25 | 24 | 27 | 25 | 36 | 35 | 42 | 32 | 25 | 26 | 25 | 36 | 34 | 35 | 31 | 56 |
| Error% | 2.03 | 2.70 | 2.56 | 2.93 | 3.29 | 4.23 | 3.92 | 5.85 | 4.40 | 3.50 | 3.54 | 3.44 | 4.16 | 3.94 | 4.09 | 3.51 | 7.85 |
| Cations | | | | | | | | | | | | | | | | | |
| P | 0.794 | 0.885 | 0.870 | 0.901 | 0.908 | 0.955 | 0.945 | 0.956 | 0.914 | 0.926 | 0.920 | 0.915 | 0.956 | 0.948 | 0.957 | 0.938 | 0.979 |
| Si | 0.212 | 0.123 | 0.137 | 0.105 | 0.107 | 0.063 | 0.069 | 0.055 | 0.079 | 0.103 | 0.102 | 0.106 | 0.066 | 0.075 | 0.068 | 0.086 | 0.039 |
| Th | 0.263 | 0.156 | 0.172 | 0.137 | 0.133 | 0.086 | 0.092 | 0.067 | 0.099 | 0.133 | 0.126 | 0.131 | 0.088 | 0.098 | 0.092 | 0.111 | 0.047 |
| U | 0.001 | 0.001 | 0.001 | 0.001 | 0.001 | 0.001 | 0.001 | 0.001 | 0.001 | 0.001 | 0.001 | 0.001 | 0.001 | 0.001 | 0.001 | 0.001 | 0.001 |
| Al | 0.004 | 0.003 | 0.003 | 0.003 | 0.003 | 0.001 | 0.002 | 0.001 | 0.002 | 0.002 | 0.001 | 0.002 | 0.002 | 0.002 | 0.002 | 0.001 | 0.001 |
| Y | 0.002 | 0.002 | 0.002 | 0.001 | 0.003 | 0.002 | 0.002 | 0.003 | 0.003 | 0.003 | 0.003 | 0.003 | 0.002 | 0.002 | 0.002 | 0.002 | 0.004 |
| La | 0.168 | 0.205 | 0.199 | 0.209 | 0.188 | 0.210 | 0.216 | 0.219 | 0.221 | 0.186 | 0.190 | 0.185 | 0.211 | 0.213 | 0.207 | 0.201 | 0.215 |
| Ce | 0.319 | 0.385 | 0.378 | 0.400 | 0.392 | 0.424 | 0.422 | 0.440 | 0.432 | 0.376 | 0.387 | 0.383 | 0.415 | 0.408 | 0.406 | 0.400 | 0.445 |
| Pr | 0.033 | 0.040 | 0.038 | 0.041 | 0.041 | 0.043 | 0.043 | 0.046 | 0.044 | 0.043 | 0.043 | 0.043 | 0.045 | 0.043 | 0.044 | 0.043 | 0.047 |
| Nd | 0.111 | 0.129 | 0.127 | 0.135 | 0.150 | 0.149 | 0.144 | 0.160 | 0.154 | 0.144 | 0.151 | 0.152 | 0.146 | 0.142 | 0.148 | 0.144 | 0.168 |
| Gd | 0.007 | 0.007 | 0.006 | 0.007 | 0.009 | 0.008 | 0.009 | 0.009 | 0.008 | 0.009 | 0.009 | 0.010 | 0.008 | 0.007 | 0.008 | 0.008 | 0.009 |
| Dy | 0.002 | 0.001 | 0.001 | 0.000 | 0.001 | 0.001 | 0.001 | 0.001 | 0.001 | 0.001 | 0.001 | 0.001 | 0.001 | 0.001 | 0.001 | 0.001 | 0.001 |
| Sm | 0.014 | 0.015 | 0.015 | 0.016 | 0.021 | 0.020 | 0.018 | 0.021 | 0.019 | 0.020 | 0.021 | 0.020 | 0.018 | 0.018 | 0.019 | 0.019 | 0.023 |
| Eu | 0.000 | 0.000 | 0.000 | 0.000 | 0.001 | 0.000 | 0.000 | 0.001 | 0.000 | 0.000 | 0.001 | 0.002 | 0.000 | 0.000 | 0.001 | 0.001 | 0.001 |
| Ca | 0.066 | 0.048 | 0.050 | 0.043 | 0.039 | 0.032 | 0.034 | 0.023 | 0.034 | 0.038 | 0.037 | 0.038 | 0.034 | 0.035 | 0.034 | 0.037 | 0.020 |
| Pb | 0.013 | 0.008 | 0.008 | 0.007 | 0.005 | 0.004 | 0.004 | 0.003 | 0.004 | 0.005 | 0.005 | 0.005 | 0.004 | 0.004 | 0.004 | 0.005 | 0.002 |
| Total | 2.010 | 2.007 | 2.007 | 2.007 | 2.003 | 1.999 | 2.002 | 2.004 | 2.016 | 1.992 | 1.998 | 1.999 | 1.997 | 1.995 | 1.994 | 1.996 | 2.001 |
| $X_{Hutt.}$ | 0.211 | 0.118 | 0.133 | 0.102 | 0.102 | 0.059 | 0.064 | 0.048 | 0.069 | 0.105 | 0.097 | 0.102 | 0.061 | 0.071 | 0.066 | 0.082 | 0.030 |
| $X_{Cher.}$ | 0.133 | 0.096 | 0.100 | 0.087 | 0.079 | 0.066 | 0.069 | 0.046 | 0.066 | 0.079 | 0.076 | 0.077 | 0.070 | 0.072 | 0.070 | 0.075 | 0.041 |
| $X_{Mon.}$ | 0.656 | 0.786 | 0.768 | 0.811 | 0.819 | 0.874 | 0.867 | 0.906 | 0.865 | 0.816 | 0.827 | 0.820 | 0.869 | 0.858 | 0.864 | 0.842 | 0.929 |

Table 1. Continued

| | Grain iv | | | | | | | | | | | | | | |
|---|---|---|---|---|---|---|---|---|---|---|---|---|---|---|---|
| | rim | rim | rim | rim | rim | core | core | core | core | core | core | core | core | core | core |
| $P_2O_5$ | 27.31 | 27.69 | 29.80 | 29.55 | 28.29 | 22.92 | 22.38 | 21.71 | 29.80 | 26.04 | 23.43 | 21.92 | 21.65 | 24.84 | 25.35 |
| $SiO_2$ | 2.53 | 2.22 | 0.93 | 0.93 | 1.27 | 4.19 | 5.42 | 5.80 | 1.07 | 3.19 | 4.61 | 5.56 | 5.58 | 3.89 | 3.66 |
| $ThO_2$ | 14.23 | 12.50 | 4.39 | 4.60 | 6.64 | 20.07 | 29.16 | 30.76 | 10.07 | 20.76 | 26.37 | 29.26 | 28.79 | 23.80 | 22.87 |
| $UO_2$ | 0.11 | 0.11 | 0.06 | 0.06 | 0.09 | 0.11 | 0.11 | 0.10 | 0.09 | 0.08 | 0.12 | 0.10 | 0.11 | 0.12 | 0.11 |
| $Al_2O_3$ | 0.05 | 0.04 | 0.01 | 0.01 | 0.02 | 0.13 | 0.09 | 0.10 | 0.04 | 0.07 | 0.08 | 0.10 | 0.11 | 0.08 | 0.08 |
| $Y_2O_3$ | 0.09 | 0.08 | 0.12 | 0.12 | 0.12 | 0.09 | 0.10 | 0.08 | 0.14 | 0.17 | 0.13 | 0.09 | 0.08 | 0.14 | 0.15 |
| $La_2O_3$ | 13.67 | 14.04 | 15.04 | 14.92 | 14.76 | 11.64 | 10.11 | 9.73 | 13.48 | 11.32 | 10.42 | 9.99 | 10.21 | 10.89 | 11.14 |
| $Ce_2O_3$ | 27.16 | 28.00 | 31.66 | 31.53 | 30.47 | 23.56 | 20.19 | 19.37 | 28.08 | 23.34 | 20.99 | 19.93 | 20.28 | 22.13 | 22.63 |
| $Pr_2O_3$ | 2.77 | 2.84 | 3.21 | 3.15 | 3.13 | 2.40 | 2.11 | 2.01 | 2.81 | 2.40 | 2.21 | 2.19 | 2.10 | 2.33 | 2.32 |
| $Nd_2O_3$ | 9.80 | 10.28 | 12.41 | 12.01 | 11.43 | 8.88 | 7.60 | 7.23 | 10.84 | 8.90 | 7.87 | 7.29 | 7.52 | 8.42 | 8.49 |
| $Gd_2O_3$ | 0.45 | 0.51 | 0.60 | 0.67 | 0.60 | 0.34 | 0.35 | 0.44 | 0.58 | 0.57 | 0.39 | 0.43 | 0.38 | 0.44 | 0.42 |
| $Dy_2O_3$ | 0.03 | 0.04 | 0.06 | 0.09 | 0.03 | 0.07 | 0.07 | 0.06 | 0.05 | 0.07 | 0.09 | 0.04 | 0.07 | 0.07 | 0.10 |
| $Sm_2O_3$ | 1.09 | 1.15 | 1.38 | 1.38 | 1.36 | 1.02 | 0.87 | 0.81 | 1.39 | 1.00 | 0.90 | 0.86 | 0.81 | 1.01 | 1.05 |
| $Eu_2O_3$ | 0.03 | 0.07 | 0.11 | 0.17 | 0.10 | 0.05 | 0.02 | 0.05 | 0.05 | 0.05 | 0.00 | 0.01 | 0.02 | 0.05 | 0.09 |
| CaO | 0.98 | 0.89 | 0.41 | 0.44 | 0.61 | 1.26 | 1.50 | 1.52 | 1.47 | 1.81 | 1.71 | 1.53 | 1.59 | 1.81 | 1.82 |
| PbO | 0.60 | 0.53 | 0.15 | 0.15 | 0.21 | 0.75 | 1.22 | 1.27 | 0.44 | 0.86 | 1.09 | 1.20 | 1.15 | 1.00 | 0.96 |
| Total | 100.83 | 100.93 | 100.26 | 99.69 | 99.05 | 97.43 | 101.20 | 101.00 | 100.30 | 100.58 | 100.40 | 100.45 | 100.40 | 100.98 | 101.20 |
| Age (Ma) | 954 | 953 | 756 | 735 | 710 | 860 | 963 | 952 | 981 | 955 | 943 | 946 | 915 | 957 | 962 |
| 2σ err | 35 | 38 | 69 | 66 | 49 | 28 | 26 | 26 | 43 | 29 | 27 | 26 | 25 | 28 | 29 |
| Error% | 3.669 | 3.987 | 9.127 | 8.98 | 6.901 | 3.256 | 2.700 | 2.731 | 4.383 | 3.037 | 2.863 | 2.748 | 2.732 | 2.926 | 3.015 |
| | | | | | | | | Cations | | | | | | | |
| P | 0.898 | 0.907 | 0.958 | 0.957 | 0.934 | 0.808 | 0.774 | 0.757 | 0.959 | 0.870 | 0.806 | 0.765 | 0.758 | 0.838 | 0.850 |
| Si | 0.098 | 0.086 | 0.035 | 0.035 | 0.049 | 0.175 | 0.221 | 0.239 | 0.041 | 0.126 | 0.187 | 0.229 | 0.231 | 0.155 | 0.145 |
| Th | 0.126 | 0.110 | 0.038 | 0.040 | 0.059 | 0.190 | 0.271 | 0.288 | 0.087 | 0.186 | 0.244 | 0.274 | 0.271 | 0.216 | 0.206 |
| U | 0.001 | 0.001 | 0.001 | 0.000 | 0.001 | 0.001 | 0.001 | 0.001 | 0.001 | 0.001 | 0.001 | 0.001 | 0.001 | 0.001 | 0.001 |
| Al | 0.002 | 0.002 | 0.000 | 0.000 | 0.001 | 0.007 | 0.004 | 0.005 | 0.002 | 0.003 | 0.004 | 0.005 | 0.005 | 0.004 | 0.004 |
| Y | 0.002 | 0.002 | 0.002 | 0.003 | 0.003 | 0.002 | 0.002 | 0.002 | 0.003 | 0.003 | 0.003 | 0.002 | 0.002 | 0.003 | 0.003 |
| La | 0.196 | 0.200 | 0.211 | 0.211 | 0.212 | 0.179 | 0.152 | 0.148 | 0.189 | 0.165 | 0.156 | 0.152 | 0.156 | 0.160 | 0.163 |
| Ce | 0.386 | 0.397 | 0.440 | 0.442 | 0.435 | 0.359 | 0.302 | 0.292 | 0.391 | 0.337 | 0.312 | 0.301 | 0.307 | 0.323 | 0.328 |
| Pr | 0.096 | 0.098 | 0.109 | 0.108 | 0.109 | 0.09 | 0.077 | 0.074 | 0.096 | 0.085 | 0.080 | 0.081 | 0.078 | 0.083 | 0.082 |
| Nd | 0.136 | 0.142 | 0.168 | 0.164 | 0.159 | 0.132 | 0.111 | 0.106 | 0.147 | 0.125 | 0.114 | 0.107 | 0.111 | 0.120 | 0.120 |
| Gd | 0.006 | 0.007 | 0.008 | 0.008 | 0.008 | 0.005 | 0.005 | 0.006 | 0.007 | 0.007 | 0.005 | 0.006 | 0.005 | 0.006 | 0.005 |
| Dy | 0.000 | 0.000 | 0.001 | 0.001 | 0.000 | 0.001 | 0.001 | 0.001 | 0.001 | 0.001 | 0.001 | 0.000 | 0.001 | 0.001 | 0.001 |
| Sm | 0.015 | 0.015 | 0.018 | 0.018 | 0.018 | 0.015 | 0.012 | 0.011 | 0.018 | 0.014 | 0.013 | 0.012 | 0.012 | 0.014 | 0.014 |
| Eu | 0.000 | 0.001 | 0.001 | 0.002 | 0.001 | 0.001 | 0.000 | 0.001 | 0.001 | 0.001 | 0.000 | 0.000 | 0.000 | 0.001 | 0.001 |
| Ca | 0.041 | 0.037 | 0.017 | 0.018 | 0.025 | 0.056 | 0.065 | 0.067 | 0.060 | 0.076 | 0.075 | 0.068 | 0.070 | 0.077 | 0.077 |
| Pb | 0.006 | 0.005 | 0.002 | 0.002 | 0.002 | 0.008 | 0.013 | 0.014 | 0.004 | 0.009 | 0.012 | 0.013 | 0.013 | 0.011 | 0.010 |
| Total | 2.009 | 2.010 | 2.009 | 2.010 | 2.017 | 2.028 | 2.013 | 2.013 | 2.006 | 2.011 | 2.014 | 2.016 | 2.021 | 2.013 | 2.012 |
| $X_{Hutt.}$ | 0.091 | 0.078 | 0.023 | 0.023 | 0.035 | 0.138 | 0.217 | 0.234 | 0.032 | 0.119 | 0.179 | 0.217 | 0.209 | 0.148 | 0.138 |
| $X_{Cher.}$ | 0.081 | 0.073 | 0.033 | 0.036 | 0.049 | 0.109 | 0.129 | 0.133 | 0.119 | 0.151 | 0.147 | 0.133 | 0.137 | 0.152 | 0.153 |
| $X_{Mon.}$ | 0.828 | 0.849 | 0.944 | 0.941 | 0.915 | 0.754 | 0.654 | 0.634 | 0.848 | 0.730 | 0.674 | 0.650 | 0.654 | 0.700 | 0.709 |

Table 1. Continued

| | Group-III monazite | | | | | | | | | | | | | | | | |
|---|---|---|---|---|---|---|---|---|---|---|---|---|---|---|---|---|---|
| | Grain v | | | | | | | | | | | | | | | | |
| | rim | rim | rim | rim | core | core | core | core | core | core | core | core | core | core | core | core | core |
| $P_2O_5$ | 26.98 | 27.42 | 27.74 | 27.46 | 23.47 | 24.28 | 23.66 | 26.14 | 27.00 | 26.65 | 27.11 | 28.65 | 26.77 | 27.32 | 26.43 | 26.71 | 28.99 |
| $SiO_2$ | 2.32 | 2.20 | 1.96 | 2.16 | 4.51 | 3.93 | 4.40 | 2.74 | 2.21 | 2.52 | 2.10 | 1.16 | 2.40 | 2.03 | 2.37 | 2.61 | 1.23 |
| $ThO_2$ | 11.59 | 12.13 | 10.91 | 12.14 | 25.08 | 22.56 | 24.38 | 16.16 | 12.74 | 15.06 | 11.61 | 10.67 | 13.15 | 11.67 | 13.34 | 15.51 | 10.29 |
| $UO_2$ | 0.10 | 0.11 | 0.11 | 0.11 | 0.10 | 0.11 | 0.11 | 0.10 | 0.11 | 0.11 | 0.12 | 0.12 | 0.11 | 0.10 | 0.11 | 0.11 | 0.08 |
| $Al_2O_3$ | 0.04 | 0.05 | 0.03 | 0.05 | 0.10 | 0.07 | 0.08 | 0.05 | 0.04 | 0.05 | 0.04 | 0.04 | 0.05 | 0.05 | 0.04 | 0.06 | 0.04 |
| $Y_2O_3$ | 0.20 | 0.17 | 0.15 | 0.17 | 0.08 | 0.09 | 0.11 | 0.08 | 0.08 | 0.08 | 0.16 | 0.35 | 0.14 | 0.16 | 0.15 | 0.05 | 0.25 |
| $La_2O_3$ | 13.22 | 13.60 | 13.91 | 13.51 | 11.33 | 11.91 | 11.33 | 13.46 | 14.05 | 13.61 | 13.36 | 13.88 | 13.26 | 13.38 | 12.96 | 13.60 | 14.29 |
| $Ce_2O_3$ | 27.89 | 27.58 | 28.18 | 27.52 | 21.82 | 22.93 | 22.09 | 26.02 | 27.49 | 26.49 | 27.45 | 27.04 | 27.07 | 27.97 | 27.03 | 25.89 | 27.66 |
| $Pr_2O_3$ | 3.05 | 2.89 | 2.76 | 2.87 | 2.30 | 2.37 | 2.31 | 2.65 | 2.78 | 2.68 | 2.87 | 2.87 | 2.90 | 2.90 | 2.69 | 2.68 | 2.82 |
| $Nd_2O_3$ | 11.42 | 11.52 | 11.59 | 11.37 | 8.00 | 8.19 | 8.10 | 9.33 | 10.08 | 9.61 | 10.80 | 10.15 | 10.67 | 11.72 | 11.24 | 9.74 | 11.02 |
| $Gd_2O_3$ | 0.73 | 0.56 | 0.57 | 0.49 | 0.45 | 0.49 | 0.45 | 0.39 | 0.51 | 0.49 | 0.64 | 0.74 | 0.62 | 0.49 | 0.54 | 0.47 | 0.61 |
| $Dy_2O_3$ | 0.13 | 0.06 | 0.09 | 0.08 | 0.07 | 0.07 | 0.13 | 0.07 | 0.08 | 0.02 | 0.06 | 0.15 | 0.10 | 0.09 | 0.05 | 0.08 | 0.08 |
| $Sm_2O_3$ | 1.52 | 1.37 | 1.29 | 1.35 | 0.94 | 0.98 | 0.89 | 1.07 | 1.19 | 1.08 | 1.41 | 1.41 | 1.34 | 1.33 | 1.23 | 1.03 | 1.31 |
| $Eu_2O_3$ | 0.18 | 0.10 | 0.07 | 0.11 | 0.06 | 0.03 | 0.05 | 0.11 | 0.04 | 0.13 | 0.12 | 0.11 | 0.12 | 0.07 | 0.02 | 0.00 | 0.00 |
| CaO | 0.59 | 0.86 | 0.83 | 0.87 | 1.60 | 1.56 | 1.56 | 1.26 | 1.02 | 1.22 | 0.86 | 1.53 | 0.86 | 0.83 | 0.87 | 1.23 | 1.35 |
| PbO | 0.42 | 0.41 | 0.36 | 0.42 | 1.03 | 0.93 | 0.97 | 0.63 | 0.52 | 0.62 | 0.39 | 0.46 | 0.43 | 0.39 | 0.41 | 0.59 | 0.43 |
| Total | 100.31 | 100.95 | 100.49 | 100.60 | 100.86 | 100.44 | 100.56 | 100.19 | 99.89 | 100.33 | 99.01 | 99.26 | 99.93 | 100.43 | 99.44 | 100.30 | 100.37 |
| Age (Ma) | 830 | 770 | 753 | 779 | 938 | 944 | 911 | 890 | 923 | 932 | 753 | 954 | 746 | 750 | 705 | 870 | 952 |
| 2σ err | 36 | 34 | 36 | 34 | 27 | 28 | 27 | 31 | 36 | 33 | 35 | 41 | 32 | 34 | 31 | 32 | 41 |
| Error% | 4.337 | 4.416 | 4.781 | 4.365 | 2.878 | 2.966 | 2.964 | 3.483 | 3.9 | 3.541 | 4.648 | 4.298 | 4.29 | 4.533 | 4.397 | 3.678 | 4.307 |
| | Cations | | | | | | | | | | | | | | | | |
| P | 0.894 | 0.901 | 0.913 | 0.904 | 0.805 | 0.829 | 0.811 | 0.877 | 0.899 | 0.888 | 0.906 | 0.942 | 0.892 | 0.903 | 0.89 | 0.888 | 0.943 |
| Si | 0.091 | 0.085 | 0.076 | 0.084 | 0.183 | 0.158 | 0.178 | 0.109 | 0.087 | 0.099 | 0.083 | 0.045 | 0.095 | 0.079 | 0.094 | 0.102 | 0.047 |
| Th | 0.103 | 0.107 | 0.096 | 0.107 | 0.231 | 0.207 | 0.225 | 0.146 | 0.114 | 0.135 | 0.104 | 0.094 | 0.118 | 0.104 | 0.121 | 0.139 | 0.09 |
| U | 0.001 | 0.001 | 0.001 | 0.001 | 0.001 | 0.001 | 0.001 | 0.001 | 0.001 | 0.001 | 0.001 | 0.001 | 0.001 | 0.001 | 0.001 | 0.001 | 0.001 |
| Al | 0.002 | 0.002 | 0.002 | 0.002 | 0.005 | 0.003 | 0.004 | 0.002 | 0.002 | 0.002 | 0.002 | 0.002 | 0.002 | 0.002 | 0.002 | 0.003 | 0.002 |
| Y | 0.004 | 0.003 | 0.003 | 0.003 | 0.002 | 0.002 | 0.002 | 0.002 | 0.002 | 0.002 | 0.003 | 0.007 | 0.003 | 0.003 | 0.003 | 0.001 | 0.005 |
| La | 0.191 | 0.195 | 0.199 | 0.194 | 0.169 | 0.177 | 0.169 | 0.197 | 0.204 | 0.198 | 0.194 | 0.199 | 0.192 | 0.193 | 0.190 | 0.197 | 0.202 |
| Ce | 0.400 | 0.392 | 0.401 | 0.392 | 0.324 | 0.338 | 0.328 | 0.377 | 0.396 | 0.382 | 0.397 | 0.384 | 0.390 | 0.400 | 0.393 | 0.372 | 0.389 |
| Pr | 0.107 | 0.101 | 0.096 | 0.100 | 0.083 | 0.086 | 0.084 | 0.094 | 0.098 | 0.094 | 0.101 | 0.100 | 0.102 | 0.102 | 0.096 | 0.094 | 0.097 |
| Nd | 0.160 | 0.160 | 0.161 | 0.158 | 0.116 | 0.118 | 0.117 | 0.132 | 0.141 | 0.135 | 0.152 | 0.141 | 0.150 | 0.164 | 0.160 | 0.137 | 0.151 |
| Gd | 0.009 | 0.007 | 0.007 | 0.006 | 0.006 | 0.007 | 0.006 | 0.005 | 0.007 | 0.006 | 0.008 | 0.010 | 0.008 | 0.006 | 0.007 | 0.006 | 0.008 |
| Dy | 0.002 | 0.001 | 0.001 | 0.001 | 0.001 | 0.001 | 0.002 | 0.001 | 0.001 | 0.000 | 0.001 | 0.002 | 0.001 | 0.001 | 0.001 | 0.001 | 0.001 |
| Sm | 0.021 | 0.018 | 0.017 | 0.018 | 0.013 | 0.014 | 0.012 | 0.015 | 0.016 | 0.015 | 0.019 | 0.019 | 0.018 | 0.018 | 0.017 | 0.014 | 0.017 |
| Eu | 0.002 | 0.001 | 0.001 | 0.001 | 0.001 | 0.000 | 0.001 | 0.001 | 0.001 | 0.002 | 0.002 | 0.001 | 0.002 | 0.001 | 0.000 | 0.000 | 0.000 |
| Ca | 0.025 | 0.036 | 0.034 | 0.036 | 0.069 | 0.067 | 0.068 | 0.054 | 0.043 | 0.051 | 0.036 | 0.064 | 0.036 | 0.035 | 0.037 | 0.052 | 0.055 |
| Pb | 0.004 | 0.004 | 0.004 | 0.004 | 0.011 | 0.010 | 0.011 | 0.007 | 0.006 | 0.007 | 0.004 | 0.005 | 0.005 | 0.004 | 0.004 | 0.006 | 0.004 |
| Total | 2.015 | 2.015 | 2.013 | 2.013 | 2.019 | 2.018 | 2.018 | 2.017 | 2.017 | 2.016 | 2.014 | 2.015 | 2.015 | 2.016 | 2.016 | 2.013 | 2.012 |
| $X_{Hutt.}$ | 0.082 | 0.075 | 0.065 | 0.075 | 0.169 | 0.147 | 0.165 | 0.097 | 0.075 | 0.088 | 0.071 | 0.035 | 0.085 | 0.072 | 0.086 | 0.092 | 0.039 |
| $X_{Cher.}$ | 0.048 | 0.070 | 0.067 | 0.070 | 0.135 | 0.131 | 0.132 | 0.104 | 0.083 | 0.100 | 0.071 | 0.124 | 0.071 | 0.067 | 0.072 | 0.102 | 0.108 |
| $X_{Mon.}$ | 0.870 | 0.856 | 0.867 | 0.855 | 0.696 | 0.722 | 0.703 | 0.799 | 0.841 | 0.811 | 0.858 | 0.840 | 0.845 | 0.861 | 0.842 | 0.806 | 0.853 |

Table 1. Continued

| | Grain vi | | | | | | | | Grain vii | | | | |
|---|---|---|---|---|---|---|---|---|---|---|---|---|---|
| | rim | rim | core | core | core | core | core | | rim | rim | rim | core | core |
| $P_2O_5$ | 27.52 | 27.39 | 29.26 | 28.15 | 29.66 | 27.10 | 29.28 | $P_2O_5$ | 28.42 | 28.96 | 29.16 | 28.20 | 29.00 |
| $SiO_2$ | 2.12 | 2.16 | 1.14 | 1.64 | 0.95 | 2.37 | 1.11 | $SiO_2$ | 1.29 | 1.10 | 1.11 | 1.68 | 1.78 |
| $ThO_2$ | 10.88 | 11.03 | 9.96 | 12.89 | 9.88 | 12.11 | 10.43 | $ThO_2$ | 6.33 | 5.89 | 6.01 | 9.32 | 10.47 |
| $UO_2$ | 0.11 | 0.08 | 0.08 | 0.09 | 0.08 | 0.10 | 0.10 | $UO_2$ | 0.09 | 0.08 | 0.07 | 0.08 | 0.13 |
| $Al_2O_3$ | 0.05 | 0.04 | 0.04 | 0.05 | 0.03 | 0.04 | 0.04 | $Al_2O_3$ | 0.02 | 0.02 | 0.04 | 0.03 | 0.03 |
| $Y_2O_3$ | 0.15 | 0.14 | 0.20 | 0.22 | 0.06 | 0.16 | 0.12 | $Y_2O_3$ | 0.11 | 0.12 | 0.11 | 0.15 | 0.14 |
| $La_2O_3$ | 13.66 | 13.68 | 13.89 | 13.13 | 13.68 | 13.51 | 13.31 | $La_2O_3$ | 15.40 | 15.61 | 15.54 | 14.50 | 14.44 |
| $Ce_2O_3$ | 28.44 | 28.32 | 28.18 | 26.70 | 28.59 | 27.90 | 27.90 | $Ce_2O_3$ | 30.55 | 30.81 | 30.75 | 29.12 | 28.63 |
| $Pr_2O_3$ | 2.99 | 2.95 | 2.99 | 2.82 | 2.87 | 2.83 | 2.97 | $Pr_2O_3$ | 3.04 | 3.08 | 3.09 | 2.91 | 2.93 |
| $Nd_2O_3$ | 10.98 | 10.94 | 10.72 | 10.17 | 10.96 | 10.87 | 11.00 | $Nd_2O_3$ | 11.19 | 11.22 | 11.10 | 10.84 | 10.29 |
| $Gd_2O_3$ | 0.66 | 0.65 | 0.64 | 0.68 | 0.50 | 0.64 | 0.59 | $Gd_2O_3$ | 0.46 | 0.61 | 0.56 | 0.48 | 0.63 |
| $Dy_2O_3$ | 0.11 | 0.05 | 0.14 | 0.10 | 0.03 | 0.10 | 0.09 | $Dy_2O_3$ | 0.05 | 0.05 | 0.06 | 0.08 | 0.06 |
| $Sm_2O_3$ | 1.40 | 1.42 | 1.33 | 1.23 | 1.41 | 1.44 | 1.42 | $Sm_2O_3$ | 1.30 | 1.32 | 1.29 | 1.31 | 1.40 |
| $Eu_2O_3$ | 0.16 | 0.13 | 0.12 | 0.11 | 0.10 | 0.09 | 0.09 | $Eu_2O_3$ | 0.11 | 0.08 | 0.12 | 0.08 | 0.00 |
| CaO | 0.67 | 0.66 | 1.40 | 1.59 | 1.53 | 0.69 | 1.49 | CaO | 0.52 | 0.54 | 0.58 | 0.76 | 0.82 |
| PbO | 0.35 | 0.34 | 0.43 | 0.54 | 0.43 | 0.37 | 0.44 | PbO | 0.21 | 0.20 | 0.20 | 0.32 | 0.36 |
| Total | 100.15 | 99.926 | 100.45 | 100.04 | 100.72 | 100.2 | 100.3 | Total | 99.05 | 99.64 | 99.71 | 99.79 | 101.09 |
| Age (Ma) | 725 | 709 | 974 | 950 | 978 | 696 | 952 | Age (Ma) | 747 | 751 | 734 | 773 | 767 |
| 2σ err | 36 | 35 | 43 | 36 | 43 | 33 | 41 | 2σ err | 52 | 55 | 54 | 40 | 33 |
| Error% | 4.97 | 4.94 | 4.42 | 3.79 | 4.40 | 4.74 | 4.31 | Error% | 6.96 | 7.32 | 7.36 | 5.18 | 4.30 |
| | | | | Cations | | | | | | | Cations | | |
| P | 0.907 | 0.905 | 0.947 | 0.925 | 0.955 | 0.897 | 0.949 | P | 0.936 | 0.945 | 0.948 | 0.926 | 0.958 |
| Si | 0.082 | 0.085 | 0.044 | 0.063 | 0.036 | 0.093 | 0.043 | Si | 0.050 | 0.042 | 0.043 | 0.065 | 0.069 |
| Th | 0.096 | 0.098 | 0.087 | 0.114 | 0.086 | 0.108 | 0.091 | Th | 0.056 | 0.052 | 0.052 | 0.082 | 0.093 |
| U | 0.001 | 0.001 | 0.001 | 0.001 | 0.001 | 0.001 | 0.001 | U | 0.001 | 0.001 | 0.001 | 0.001 | 0.001 |
| Al | 0.002 | 0.002 | 0.002 | 0.002 | 0.001 | 0.002 | 0.002 | Al | 0.001 | 0.001 | 0.002 | 0.001 | 0.001 |
| Y | 0.003 | 0.003 | 0.004 | 0.005 | 0.001 | 0.003 | 0.002 | Y | 0.002 | 0.002 | 0.002 | 0.003 | 0.003 |
| La | 0.196 | 0.197 | 0.196 | 0.188 | 0.192 | 0.195 | 0.188 | La | 0.221 | 0.222 | 0.22 | 0.207 | 0.208 |
| Ce | 0.405 | 0.405 | 0.394 | 0.379 | 0.398 | 0.400 | 0.391 | Ce | 0.435 | 0.435 | 0.432 | 0.413 | 0.409 |
| Pr | 0.104 | 0.103 | 0.102 | 0.098 | 0.098 | 0.099 | 0.102 | Pr | 0.106 | 0.106 | 0.106 | 0.101 | 0.042 |
| Nd | 0.153 | 0.153 | 0.146 | 0.141 | 0.149 | 0.152 | 0.15 | Nd | 0.155 | 0.154 | 0.152 | 0.15 | 0.143 |
| Gd | 0.008 | 0.008 | 0.008 | 0.009 | 0.006 | 0.008 | 0.008 | Gd | 0.006 | 0.008 | 0.007 | 0.006 | 0.008 |
| Dy | 0.001 | 0.001 | 0.002 | 0.001 | 0.000 | 0.001 | 0.001 | Dy | 0.001 | 0.001 | 0.001 | 0.001 | 0.001 |
| Sm | 0.019 | 0.019 | 0.017 | 0.016 | 0.018 | 0.019 | 0.019 | Sm | 0.017 | 0.017 | 0.017 | 0.018 | 0.020 |
| Eu | 0.002 | 0.002 | 0.002 | 0.001 | 0.001 | 0.001 | 0.001 | Eu | 0.001 | 0.001 | 0.002 | 0.001 | 0.000 |
| Ca | 0.028 | 0.027 | 0.057 | 0.066 | 0.062 | 0.029 | 0.061 | Ca | 0.022 | 0.022 | 0.024 | 0.031 | 0.034 |
| Pb | 0.004 | 0.004 | 0.004 | 0.006 | 0.004 | 0.004 | 0.005 | Pb | 0.002 | 0.002 | 0.002 | 0.003 | 0.004 |
| Total | 2.013 | 2.012 | 2.013 | 2.015 | 2.012 | 2.012 | 2.011 | Total | 2.015 | 2.013 | 2.011 | 2.011 | 1.993 |
| $X_{\text{Hutt.}}$ | 0.071 | 0.073 | 0.034 | 0.053 | 0.028 | 0.082 | 0.034 | $X_{\text{Hutt.}}$ | 0.036 | 0.031 | 0.031 | 0.054 | 0.066 |
| $X_{\text{Cher.}}$ | 0.055 | 0.054 | 0.113 | 0.129 | 0.123 | 0.057 | 0.120 | $X_{\text{Cher.}}$ | 0.042 | 0.043 | 0.047 | 0.062 | 0.071 |
| $X_{\text{Mon.}}$ | 0.874 | 0.873 | 0.854 | 0.818 | 0.850 | 0.861 | 0.846 | $X_{\text{Mon.}}$ | 0.922 | 0.925 | 0.922 | 0.885 | 0.863 |

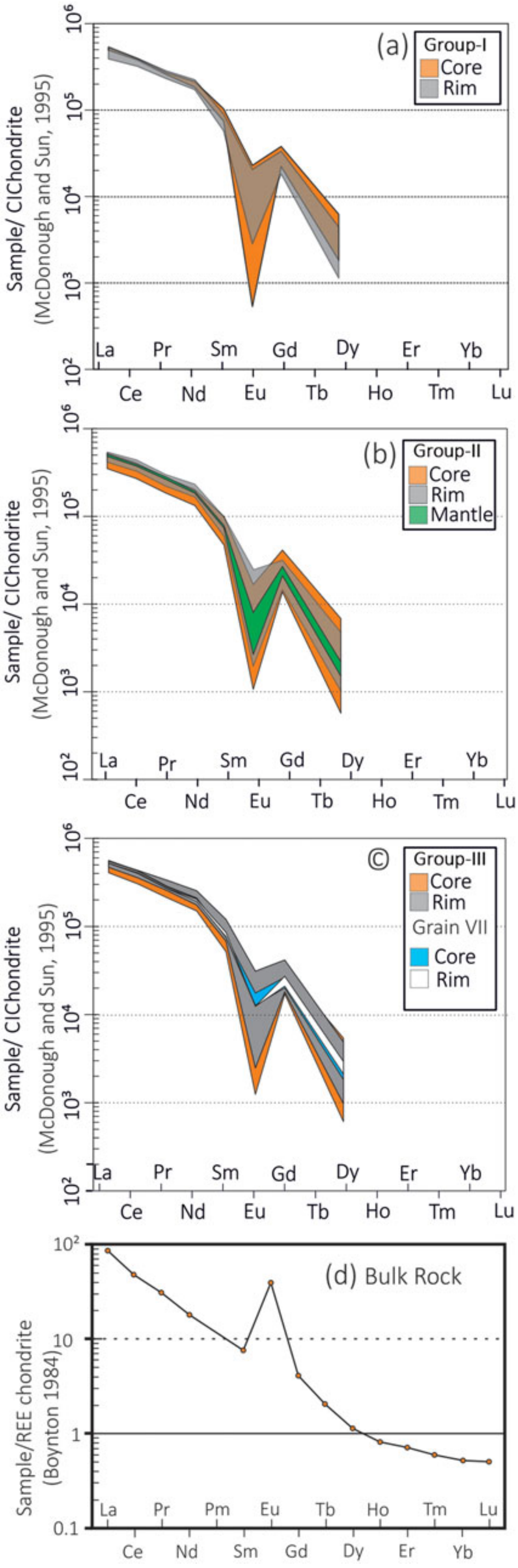

Figure 6. (Colour online) CI-chondrite (McDonough & Sun, 1995) normalized REE spider plots for (a) group-I, (b) group-II and (c) group-III monazites, and (d) the bulk rock of the monazite-bearing sample.

grains (100–200 µm in diameter) are circular to elliptical in shape; these grains are chemically zoned, with $ThO_2$-rich cores (16.73–29.16 wt %) laced by mantles having lower $ThO_2$ contents (9.60–14.73 wt %), and outermost irregular rims having even lower $ThO_2$ contents of 4.39–9.5 wt % (grains iii, iv in Fig. 5b, c). These variations taken together constitute reverse zonation in group-II monazites (Zhu & O'Nions, 1999*b*). Although rare, some of the group-II grains exhibit small and embayed dark-shaded low-$ThO_2$ domains (∼10.07 wt %) within the high-$ThO_2$ core (grain iv in Fig. 5b, c).

Monazites in the polygonized plagioclase matrix (group-III) are variable in size (50–500 µm diameter) and are characterized by patchy (grains v, vi in Fig. 5c) and reverse zoning (grain vii in Fig. 5c). In the monazites with patchy zoning, $ThO_2$ content varies from 12–25 wt % in the brighter domains to 5–10 wt % in the relatively darker domain near the margin (grains v, vi in Fig. 5b). In the monazite grains with reverse zoning, $ThO_2$ contents vary between 9 and 10 wt % in the central part and 5–6 wt % in the margins (grain vii in Fig. 5b), broadly overlapping with patchy zones in the group-III monazites. In CI-chondrite normalized (McDonough & Sun, 1995) plots, the REE contents in the monazites broadly overlap and exhibit pronounced negative Eu anomalies (Fig. 6a–c).

The compositional variations in monazites can be explained in terms of the following end-members: (a) La–Ce–Nd monazite $(La, Ce, Nd)PO_4$, (b) cheralite $(2REE^{3+} = Ca^{2+} + Th^{4+})$ and (c) huttonite $(P^{5+} + REE^{3+} = Si^{4+} + Th^{4+})$. In ternary plots after Linthout (2007), the chemical compositions of the core and rim of group-I monazites plot in the La–Ce–Nd monazite field where the $ThO_2$-rich rims show relatively higher huttonite substitution compared to the cores of the group-I monazites (Fig. 7a). For the group-II monazites, most of the core compositions plot towards the huttonite ($ThSiO_4$) end-member within the La–Ce–Nd monazite field and the chemical compositions of the mantle and marginal parts concentrate near the La–Ce–Nd monazite end-member (Fig. 7b). The chemical compositions of the matrix monazites showing patchy (grains v and vi in Fig. 5b) and Th-poorer zoning (grain vii in Fig. 5b) plot in the monazite field, varying from a huttonite-rich central part to a huttonite-poor marginal part (Fig. 7c).

The huttonite substitution in monazites could be explained in the plot of (P + Y + REE) versus (Th + U + Si) content where monazite compositions are clustered at higher (Th + U + Si) values than cheralite (Fig. 7d). Similarly, a plot of Si against (Th + U − Ca) also suggests that the chemical variations in monazite (Fig. 7e) are imparted by huttonite substitution, which usually occurs in high-temperature igneous rocks (Zhu & O'Nions, 1999*b*; Broska, Petrík & Williams, 2000; Hoshino, Watanabe & Ishihara, 2012).

## 5. Monazite chemical ages

Monazite with $ThO_2$ content > 3.5 wt % was selected for geochronological studies to reduce the $2\sigma$ error in spot age calculation (Prabhakar, 2013). A total of 133 spot analyses in monazite yielded weighted mean ages between 939 ± 5 Ma and 574 ± 19 Ma (Fig. 8a). In the probability density plot (Ludwig, 2012), the spot ages can be grouped into four populations. The mean value for the oldest age populations retrieved from group-I (grains i, ii), group-II (grains iii, iv) and group-III (grains v, vi) monazite cores is 939 ± 5 Ma. The chemical ages between 840 and 900 Ma (weighted mean 877 ± 5 Ma) are obtained in mantles surrounding the cores of group-II monazites and in patchy

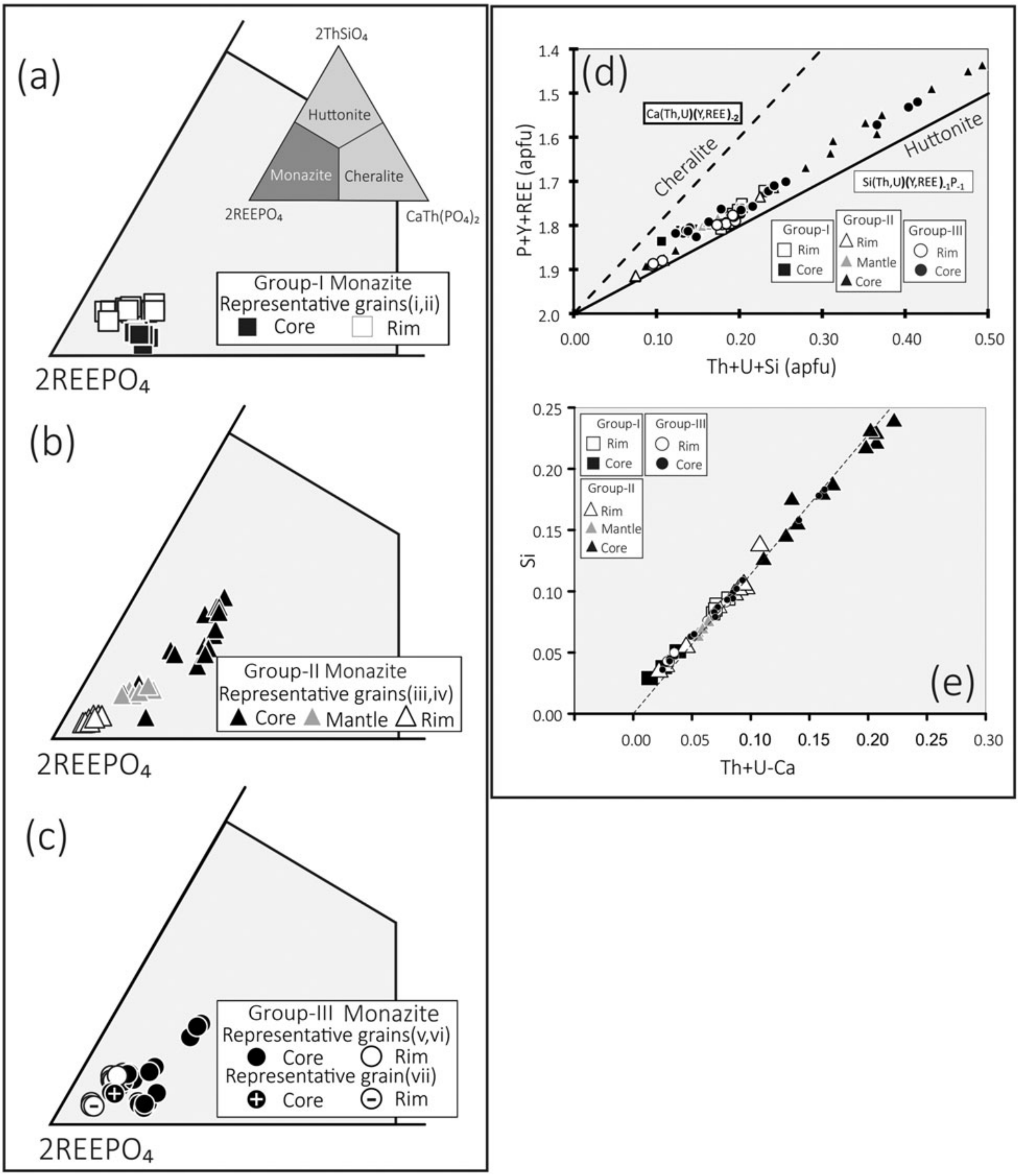

Figure 7. Plot after Linthout (2007) showing compositional variation in (a) group-I monazite, (b) group-II monazite and (c) group-III monazite. (d) (P + Y + REE) versus (Th + U + Si) and (e) Si versus (Th + U − Ca) plots of monazites.

domains of group-III monazites (grains iii–v, vii in Fig. 5). The third set of younger ages (700–780 Ma) with a mean value at 749 ± 18 Ma are retrieved from chemical domains that occur as discontinuous rims with variable thickness surrounding the 877 ± 5 Ma mantle in group-II monazites and in outer patchy domains in group-III monazites (grains iii–v, vii in Fig. 5). The Early Cambrian/Late Neoproterozoic age cluster (mean value 574 ± 19 Ma) is obtained in chemical domains that occur along fractures and extremities in monazites (grain ii in Fig. 5b).

The key to unmix polygenetic monazite ages obtained from EPMA depends on the chemical heterogeneity in texturally constrained monazite (Montel *et al.* 1996; Williams, Jercinovic & Terry, 1999) as the chemical variations in a population of monazites have little influence on the calculation of average age based on the histogram method (Ludwig, 2012). $ThO_2$* (Suzuki & Adachi, 1991*a*,*b*) against PbO is plotted to validate the selection of populations from the histogram distribution (Fig. 8b). In a closed system, if a homogeneous population of monazites contains the same amount of initial lead and a different amount of Th and U, the analytical data should define a straight line with the equation $PbO = m * ThO_2 + c$ where $m$ is the slope of the line and $c$ is the initial concentration

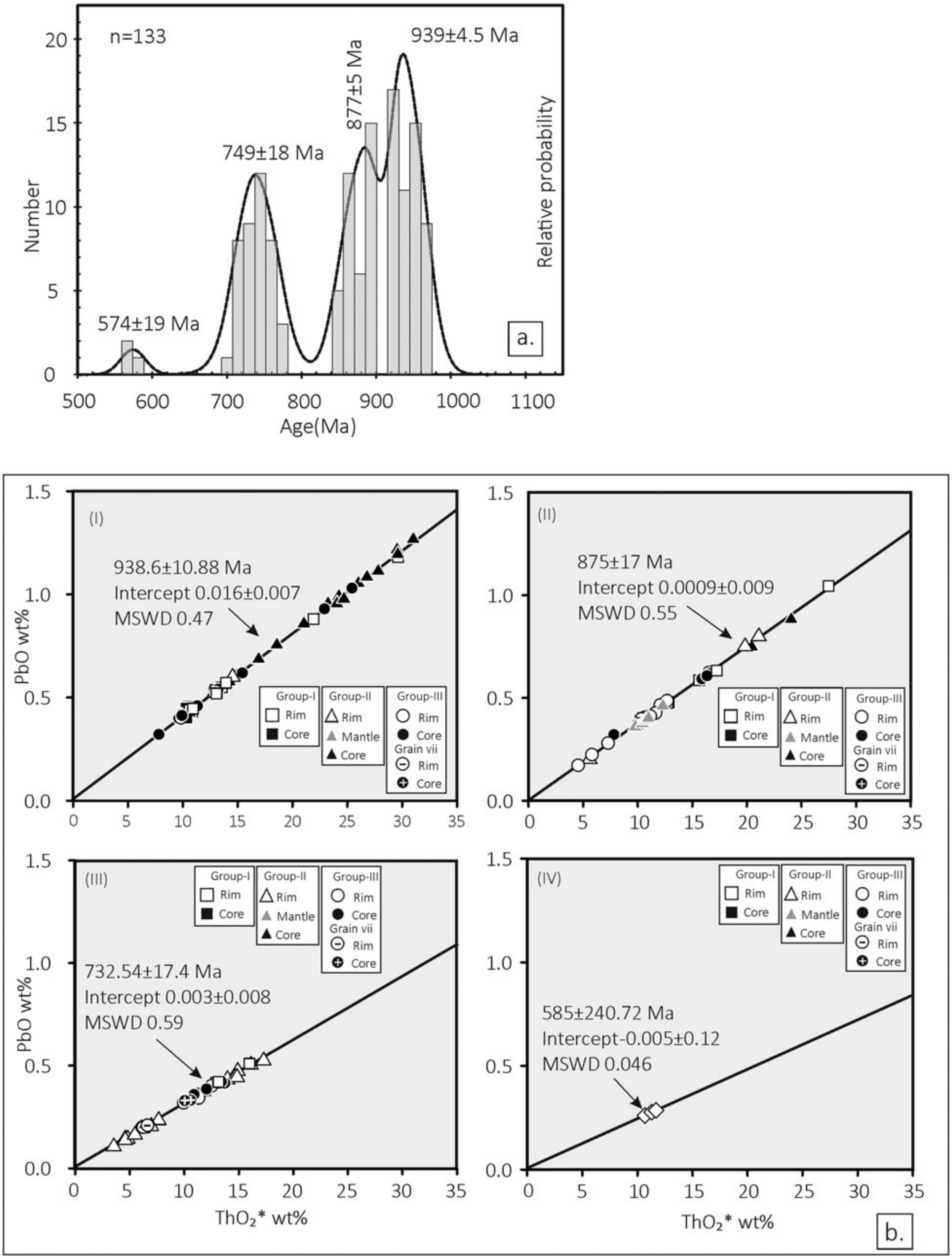

Figure 8. (a) Probability density plot of chemical ages in all monazites taken together (n = total number of spot ages). The values of unmixed ages from each population are also shown. A complete list of analyses from different domains of monazites is given in online Supplementary Material Table S1 and Figure S1 available at http://journals.cambridge.org/geo. (b) PbO versus $ThO_2$* plot of the four age populations along with regressed isochron ages.

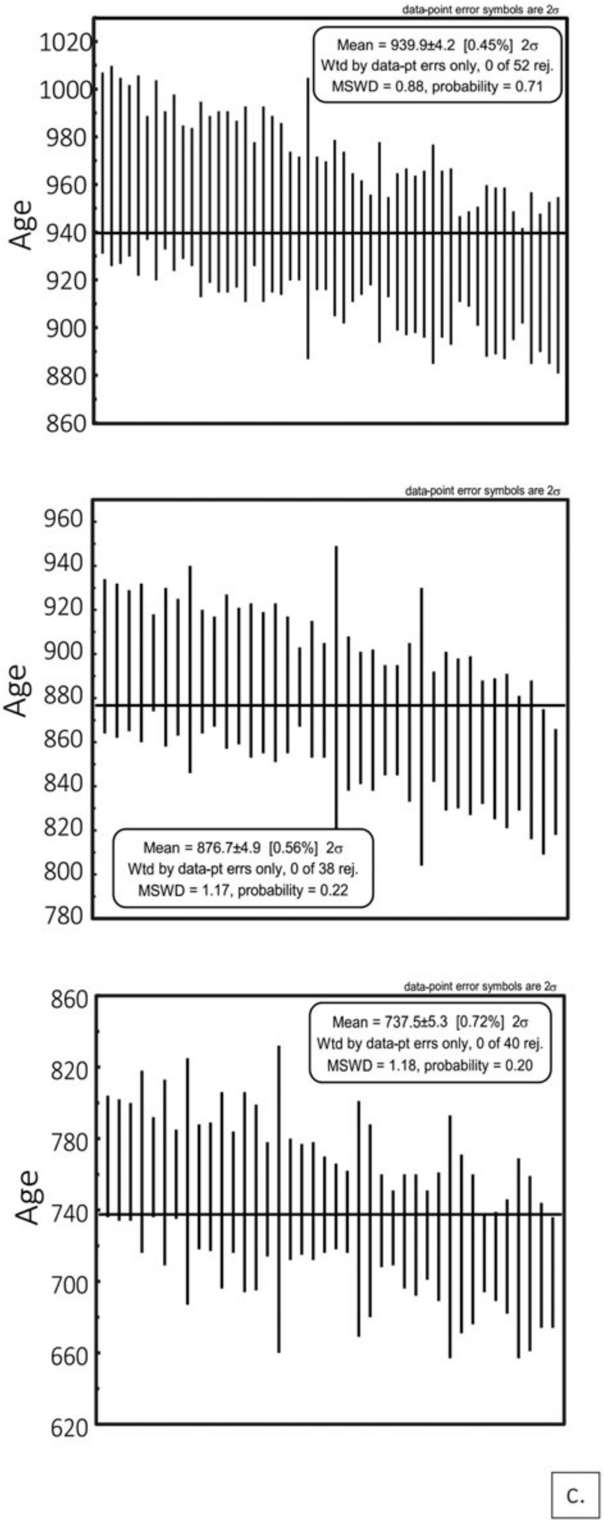

Figure 8. (Continued) (c) The weighted average age calculated using Isoplot for the three statistically different age groups.

of non-radiogenic PbO (Suzuki & Kato, 2008). Since the initial Pb content in the monazite is negligible (Parrish, 1990), the intercept of the best-fit line for a texturally constrained monazite group should be close to zero. The U–Th–$Pb_{total}$ chemical ages and associated MSWD were calculated using the CHIME program (Kato, Suzuki & Adachi, 1999).

In the PbO against ThO$_2$* plot (Fig. 8b), the chemical compositions of the monazites in the Koraput anorthosite fall into four distinct age groups with regressed isochron ages of 938.6 ± 10.88 Ma (MSWD = 0.47), 875 ± 17 Ma (MSWD = 0.55), 732.54 ± 17.4Ma (MSWD = 0.59) and 585 ± 240 Ma (MSWD 0.046). The spot ages obtained from the core and rim in group-I monazites define the 938.6 ± 10.88 Ma isochron (MSWD = 0.47, Fig. 8bi). The chemical ages obtained from the core of group-II and group-III monazites also fall in the 938 ± 10 Ma isochron. Chemical ages obtained from the moderate ThO$_2$-rich mantles in group-II monazites (grains iii, iv) and isolated patchy domains in the central and marginal parts of group-III monazites define the 875 ± 17 Ma (MSWD = 0.55) isochron (Fig. 8bii). Barring a single analysis obtained from the rim of a group-I monazite (883 ± 32 Ma, grain ii in Fig. 5c), spot ages ranging from 840–900 Ma (obtained from Fig. 5b) are absent in group-I monazites (Fig. 8bii). The 732.54 ± 17.4 Ma (MSWD = 0.59) isochron is defined by the chemical ages in the low-ThO$_2$ rims of group-II monazites, from domains showing patchy zoning of group-III monazites (grains v, vi) and from ages obtained from the core and rim of reversely zoned monazites (Fig. 8biii). The 585 ± 240.72 Ma (MSWD = 0.046) isochron is defined by ages obtained near fractures from group-II monazites (Fig. 8biv). The four isochrons pass through the origin suggesting the presence of four distinct statistically separable groups of monazite ages. However, the isochron with an age value of 585 ± 240.72 Ma (MSWD = 0.046) and the corresponding dataset is excluded owing to large errors and a limited amount of data. The following weighted average ages (a) 939.9 ± 4.2 Ma (MSWD = 0.88), (b) 876.7 ± 4.9 Ma (MSWD = 1.17) and (c) 737.5 ± 5.3 Ma (MSWD = 1.18) calculated using Isoplot 3.75 (Ludwig, 2012) are statistically separable and are in good agreement with the unmixed ages (Fig. 8a, c).

## 6. Discussion

The following features suggest that the ∼ 930 Ma group-I monazites crystallized from melts: e.g. their occurrence within magmatic orthopyroxene (grains i–iv in Fig. 5a) and plagioclase grains (grains v–vii in Fig. 5a), sharp concentric chemical zones (Williams, Jercinovic & Hetherington, 2007), high-ThO$_2$ contents (Schandl & Gorton, 2004), a steady decrease in LREE (La) to MREE (Sm) contents, and a prominent negative Eu anomaly (Zhu & O'Nions, 1999*a*). By analogy, the Early Neoproterozoic high-Th cores in group-II (grains iii, iv) and group-III monazites (grain v, vi), monazites hosted within magmatic orthopyroxene and plagioclase, respectively are also formed at similar supra-solidus conditions. Experimental data on Th partitioning in monazite–silicate melt equilibrium indicate that Th contents in monazites negatively correlate with crystallization temperature (Stepanov *et al.* 2012; Xing, Trail & Watson, 2013) and positively correlate with increasing SiO$_2$ contents in co-existing melt (Xing, Trail & Watson, 2009). By implication, the group-I monazites with a low-ThO$_2$ core and high-ThO$_2$ rim may have crystallized from magma parental to the Koraput anorthosite complex. The group-II monazites with Th-rich cores mantled by concentric zones having successively lower Th contents may have crystallized from melts (Williams, Jercinovic & Hetherington, 2007) or precipitated from fluid reservoirs albeit under a different set of physiochemical conditions compared to the group-I monazites.

A combination of the following possibilities may have led to the Th zoning observed in the younger rims in the group-II monazites hosted in magmatic grains. First, the emplacement of the neighbouring Koraput silica-undersaturated alkaline complex at 869 ± 7 Ma (Hippe *et al.* 2015) may have acted as an additional heat source and/or may have led to a

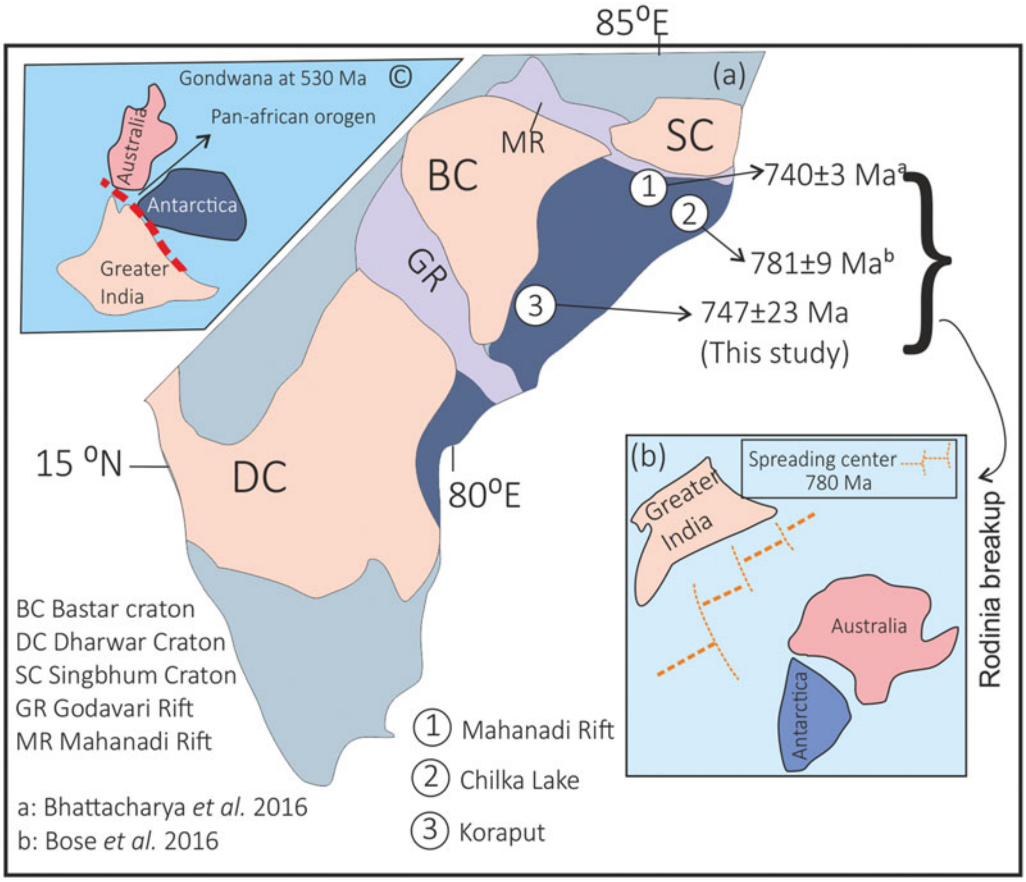

Figure 9. (Colour online) (a) Locations of mid-Neoproterozoic ages in the EGGB. Relative positions of India, Australia and Antarctica following Li *et al.* (2008) at (b) 780 Ma and (c) 530 Ma.

decrease in the Si contents via interaction with fluids, and this may have led to the precipitation of low-Th rims in group-II monazites. Second, the proximity of mineralogically altered zones in deformed pyroxenes and group-II monazites points to sub-solidus fluid activity that contributed to monazite growth. Several authors (Rasmussen & Muhling, 2007; Hetherington, Harlov & Budzyń, 2010; Harlov & Hetherington, 2010) suggested that high-temperature (magmatic) monazites are usually unstable at a lower temperature and decompose to low-Th monazites by releasing Y, Th and U (Rasmussen & Muhling, 2007). Thus, the low-$ThO_2$ rims (4.3–5.3 wt %) with irregular outlines cross-cutting the concentric magmatic zones in group-II monazites (Fig. 5, grains iii, iv) probably suggest sub-solidus monazite growth. The patchy zoning in the matrix monazites (grains v, vi in Fig. 5b) points to chemical alteration due to magmatic fluids (Fitzsimons, Kinny & Harley, 1997) or hydrothermal alteration along fractures (Townsend *et al.* 2000).

The oldest age population (mean 939 ± 5 Ma) in monazites hosted within dynamically recrystallized orthopyroxene and plagioclase correlates favourably with the emplacement ages of anorthosite plutons in the EGP at Chilka Lake (983 ± 2.5 Ma, Chatterjee *et al.* 2008), Bolangir (933 ± 32 Ma, Krause *et al.* 2001), Turkel (980 ± 8 Ma, Raith *et al.* 2014) and Jugsaipatna (984 ± 10 Ma, Dharma Rao, Santosh & Zhang, 2014*b*). The emplacement age of the anorthosites (mean 939 ± 5 Ma) and the bordering granitoids (mangerite–charnockite–granite suites; Bhattacharya *et al.* 1998) in the EGP coincides with the emplacement (980–960 Ma) of voluminous charnockite–enderbite plutons in isotopic Domain 2 (Paul *et al.* 1990; Bose *et al.* 2011) and the ultra-high-temperature (UHT) metamorphic event in the province (1000–900 Ma, Sengupta *et al.* 1990) in the EGGB. The evidence, taken together, suggests a Grenvillian-age back-arc setting for the EGP granulites. The 877 ± 5 Ma chemical ages in the Th-rich cores in the group-II monazites coincide with a U–Pb zircon age (869 ± 11 Ma) retrieved from the silica-undersaturated Koraput alkaline complex (Hippe *et al.* 2015) located close to the eastern margin of the anorthosite pluton (Fig. 2). Hippe *et al.* (2015) suggested the age corresponds with the emplacement of the nepheline syenite pluton related to the initiation of rifting in the EGGB leading to the break-up of Rodinia.

Recent age determinations along the Mahanadi Shear Zone (Bhattacharya *et al.* 2016 and references therein) and in the Chilka Lake Complex (Crowe *et al.* 2003; Bose *et al.* 2016) suggest that the northern margin of the EGP experienced a significant high-*T* (granulite facies) event in mid-Neoproterozoic time at ~750 Ma (Fig. 9a). This event was marked by extensional tectonism (Das *et al.* 2012), as opposed to crustal shortening, and may correlate with the break-up of Rodinia (Fig. 9b; Torsvik, 2003; Li *et al.* 2008). The 747 ± 23 Ma monazite age obtained from the Koraput leuconorite in this study suggests that the post-Grenvillian mid-Neoproterozoic rift-related tectonics leading to the disintegration of Rodinia may have extended along the western margin of the EGP granulites, and, by implication, this event is demonstrably more widespread than previously thought. The youngest, albeit small, population of monazite ages obtained in this study (573 ± 33 Ma) is similar to the Pan African dates retrieved from the Grenvillian-age EGP granulites and the cratonic rocks fringing the EGGB.

The accretion of the EGP with the cratonic nucleus of India is poorly constrained, although recent work seems to suggest the accretion could have occurred late in the Pan African (Dobmeier *et al.* 2006; Biswal, De Waele & Ahuja, 2007; Das *et al.* 2008; Bhattacharya *et al.* 2016) during the final assembly of Gondwanaland (Fig. 9c; Torsvik, 2003; Bhattacharya *et al.* 2016). The minor population of Pan African ages retrieved from the Koraput anorthosite possibly is a manifestation of this accretion event.

**Acknowledgements.** PN acknowledges financial support from the Science and Engineering Research Board through research project no. EMR/2014/000538. DS acknowledges the Director, IISER Bhopal for granting a fellowship for a doctoral dissertation. The authors acknowledge the detailed comments of Dr. Nilanjan Chatterjee and an anonymous reviewer; the comments went a long way in improving the content and styling of the manuscript. Editorial handling of the manuscript by Dr. Chad Deering is greatly appreciated.

## Supplementary material

To view supplementary material for this article, please visit https://doi.org/10.1017/S001675681700084X

## References

Bhattacharya, A., Das, H. H., Bell, E., Bhattacharya, A., Chatterjee, N., Saha, L. & Dutt, A. 2016. Restoration of Late Neoarchean–Early Cambrian tectonics in the Rengali orogen and its environs (eastern India): the Antarctic connection. *Lithos* **263**, 190–212.

Bhattacharya, A., Raith, M., Hoernes, S. & Banerjee, D. 1998. Geochemical evolution of the massif-type anorthosite complex at Bolangir in the Eastern Ghats Belt of India. *Journal of Petrology* **39**, 1169–95.

Bhattacharya, S., Sen, S. K. & Acharyya, A. 1994. The structural setting of the Chilka Lake granulite-migmatite-anorthosite suite with emphasis on the time relation of charnockites. *Precambrian Research* **66**, 393–409.

Biswal, T. K., De Waele, B. & Ahuja, H. 2007. Timing and dynamics of the juxtaposition of the Eastern Ghats Mobile Belt against the Bhandara craton, India: a structural and zircon U–Pb SHRIMP study of the fold-thrust belt and associated nepheline syenite plutons. *Tectonics* **26**, TC4006. doi: 10.1029/2006TC002005.

Black, L. P., Harley, S. L., Sun, S. S. & McCulloch, M. T. 1987. The Rayner Complex of East Antarctica: complex isotopic systematics with a Proterozoic mobile belt. *Journal of Metamorphic Geology* **5**, 1–26.

Bose, M. K. 1960. On garnet coronites from Koraput, Orissa. *Geological Magazine* **98**, 409–16.

Bose, M. K. 1979. On the Eastern Ghats Precambrian granulite belt and associated anorthosites. *Indian Journal Earth Science* **6**, 200–19.

Bose, S., Das, K., Torimoto, J., Arima, M. & Dunkley, D. J. 2016. Evolution of the Chilka Lake granulite complex, northern Eastern Ghats Belt, India: first evidence of ∼ 780 Ma decompression of the deep crust and its implication on the India–Antarctica correlation. *Lithos* **263**, 161–89.

Bose, S., Dunkley, D. J., Dasgupta, S., Das, K. & Arima, M. 2011. India–Antarctica–Australia–Laurentia connection in the Paleoproterozoic–Mesoproterozoic revisited: evidence from new zircon U–Pb and monazite chemical age data from the Eastern Ghats Belt, India. *Geological Society of America Bulletin* **123**, 2031–49.

Broska, I., Petrík, I. & Williams, C. T. 2000. Coexisting monazite and allanite in peraluminous granitoids of the Tribeč Mountains, Western Carpathians. *American Mineralogist* **85**, 22–32.

Boynton, W. V. 1984. Cosmochemistry of the rare earth elements: meteorite studies. In *Rare Earth Element Geochemistry, Vol. 2* (ed. P. Henderson), pp. 63–114. Amsterdam: Elsevier.

Chatterjee, N., Crowley, J. L., Mukherjee, A. & Das, S. 2008. Geochronology of the 983-Ma Chilka Lake Anorthosite, Eastern Ghats Belt, India: implications for pre-Gondwana tectonics. *The Journal of Geology* **116**, 105–18.

Chatterjee, A., Das, K., Bose, S. & Hidaka, H. 2017. Age-integrated tectonic evolution across the orogen-craton boundary: age zonation and shallow- to deep crustal participation during Late Cambrian cratonisation of Eastern Ghats Belts, India. *Lithos*, published online 4 August 2017. doi: 10.1016/j.lithos.2017.07.020

Cherniak, D. J., Watson, E. B., Grove, M. & Harrison, T. M. 2004. Pb diffusion in monazite: a combined RBS/SIMS study. *Geochimica et Cosmochimica Acta* **68**, 829–40.

Chetty, T. R. K. & Murthy, D. S. N. 1994. Collisional tectonics in the late Precambrian Eastern Ghats Mobile Belt; mesoscopic to satellite-scale structural observations. *Terra Nova* **6**, 72–81.

Crowe, W. A., Nash, C. R., Harris, L. B., Leeming, P. M. & Rankin, L. R. 2003. The geology of the Rengali Province: implications for the tectonic development of northern Orissa, India. *Journal of Asian Earth Sciences* **21**, 697–710.

Das, K., Bose, S., Karmakar, S. & Chakraborty, S. 2012. Petrotectonic framework of granulites from northern part of Chilka Lake area, Eastern Ghats Belt, India: compressional vis-à-vis transpressional tectonics. *Journal of Earth System Science* **121**, 1–17.

Das, S., Nasipuri, P., Bhattacharya, A. & Swaminathan, S. 2008. The thrust-contact between the Eastern Ghats Belt and the adjoining Baster craton (Eastern India): evidence from mafic granulites and tectonic implications. *Precambrian Research* **162**, 70–85.

Dharma Rao, C. V., Santosh, M. & Zhang, S.-H. 2014a. U–Pb zircon geochronology of ferrodiorites and quartz diorites from the Turkel Anorthosite Complex: a Neoarchaean convergent margin in eastern India. *Geological Journal* **50**, 530–8.

Dharma Rao, C. V., Santosh, M. & Zhang, S.-H. 2014b. Neoproterozoic massif type anorthosites and related magmatic suites from the Eastern Ghats Belt, India: implications for slab window magmatism at the terminal stage of collisional orogeny. *Precambrian Research* **240**, 60–78.

Dobmeier, C. J., Lütke, S., Hammerschmidt, H. & Mezger, K. 2006. Emplacement and deformation of the Vinukonda granite—implications for the geological evolution of peninsular India and for Rodinia reconstructions. *Precambrian Research* **146**, 165–78.

Dobmeier, C. J. & Raith, M. M. 2003. Crustal architecture and evolution of the Eastern Ghats Belt and adjacent regions of India. In *Proterozoic East Gondwana: Supercontinent Assembly and Breakup* (eds M. Yoshida, B. E. Windley & S. Dasgupta), pp. 145–68. Geological Society of London, Special Publication no. 206.

Dobmeier, C. J. & Simmat, R. 2002. Post-Grenvillean transpression in the Chilka Lake area, Eastern Ghats Belt—implications for the geological evolution of peninsular India. *Precambrian Research* **113**, 243–68.

Fitzsimons, I. C. W., Kinny, P. D. & Harley, S. L. 1997. Two stages of zircon and monazite growth in anatectic leucogneiss: SHRIMP constraints on the duration and intensity of Pan-African metamorphism in Prydz Bay, East Antarctica. *Terra Nova* **9**, 47–51.

Gardés, E., Jaoul, O., Montel, J. M., Seydoux-Guillame, A. M. & Wirth, R. 2006. Pb diffusion in monazite: an experimental study of $Pb^{2+} + Th^{4+} \leftrightarrow 2Nd^{3+}$ inter diffusion. *Geochimica et Cosmochimica Acta* **70**, 2325–36.

Gupta, S., Bhattacharya, A., Raith, M. & Nanda, J. K. 2000. Pressure-temperature deformation history across a vestigial craton-mobile belt boundary: the western margin of Eastern Ghats Belt at Deobhog, India. *Journal of Metamorphic Geology* **18**, 683–97.

Halpin, J. A., Gerakiteys, C. L., Clarke, G. L., Belusova, E. A. & Griffin, W. L. 2005. In-situ U–Pb geochronology and Hf isotope analyses of the Rayner complex, East Antarctica. *Contributions to Mineralogy and Petrology* **148**, 689–706.

Harley, S. L., Fitzsimons, I. C. W. & Zhao, Y. 2013. Antarctica and supercontinent evolution: historical perspectives, recent advances and unresolved issues. In *Antarctica and Supercontinent Evolution* (eds S. L. Harley, I. C. W. Fitzsimons & Y. Zhao), pp. 1–34. Geological Society of London Special Publication no. 383.

Harlov, D. E. & Hetherington, C. J. 2010. Partial high-grade alteration of monazite using alkali-bearing fluids: experiment and nature. *American Mineralogist* **95**, 1105–8.

Hetherington, C. J., Harlov, D. E. & Budzyń, B. 2010. Experimental metasomatism of monazite and xenotime: mineral stability, REE mobility and fluid composition. *Mineralogy and Petrology* **99**, 165–84.

Hippe, K., Möller, A., Quadt, A. V., Peytcheva, I. & Hammerschmidt, K. 2015. Zircon geochronology of the Koraput alkaline complex: insights from combined geochemical and U–Pb–Hf isotope analyses, and implications for the timing of alkaline magmatism in the Eastern Ghats Belt, India. *Gondwana Research* **34**, 205–20.

Hoshino, M., Watanabe, Y. & Ishihara, S. 2012. Crystal chemistry of monazite from the granitic rocks of Japan: petrographic implications. *The Canadian Mineralogist* **50**, 1331–46.

Kato, T., Suzuki, K. & Adachi, M. 1999. Computer program for the CHIME age calculation. *Journal of Earth and Planetary Sciences* **46**, 49–56.

Korhonen, F. J., Clark, C., Brown, M., Bhattacharya, S. & Taylor, R. 2013. How long-lived is ultrahigh temperature (UHT) metamorphism? Constraints from zircon and monazite geochronology in the Eastern Ghats orogenic belt, India. *Precambrian Research* **234**, 322–50.

Korhonen, F. J., Saw, A. K., Clark, C., Brown, M. & Bhattacharya, S. 2011. New constraints on UHT metamorphism in the Eastern Ghats Province through the application of phase equilibria modelling and in situ geochronology. *Gondwana Research* **20**, 764–81.

Krause, O., Dobmier, C., Raith, M. M. & Mezger, K. 2001. Age of emplacement of massif-type anorthosites in the Eastern Ghats Belt, India: constraints from U–Pb zircon dating and structural studies. *Precambrian Research* **109**, 25–38.

Lackey, J. S., Hinke, H. J. & Valley, J. W. 2002. Tracking contamination in felsic magma chambers with $\delta^{18}O$ of magmatic garnet and zircon. *Extended Abstracts, Geochimica et Cosmochimica Acta* **66** (Suppl. 1), 428.

Leelanandam, C. & Reddy, N. M. 1988. Precambrian anorthosites from Peninsular India – problems & perspectives. *Indian Journal of Geology* **60**, 111–36.

Li, Z. X., Bogdanova, S. V., Collins, A. S., Davidson, A., Waele, B. D., Ernst, R. E., Fitzsimons, I. C. W., Fuck, R. A., Gladkochub, D. P., Jacobs, J., Karlstrom, K. E., Lu, S., Natapov, L. M., Pease, V., Pisarevsky, S. A., Thrane, K. & Vernikovsky, V. 2008. Assembly, configuration, and break-up history of Rodinia: a synthesis. *Precambrian Research* **160**, 179–210.

Linthout, K. 2007. Tripartite division of the system 2REE(PO)$_4$-CaTh(PO4)$_2$-2ThSiO4 discreditation of brabantite, and recognition of cheralite as the name for members dominated by CaTh (PO$_4$)$_2$ . *Canadian Mineralogist* **45**, 503–8.

Ludwig, K. R. 2012. *Isoplot 3.75: A Geochronological Toolkit for Microsoft Excel*. Berkeley, California: Berkeley Chronological Center, Special Publication 5.

Mahapatro, S. N., Nanda, J. K. & Tripathy, A. K. 2010. The Jugsaipatna Anorthosite Complex, Eastern Ghats Belt, India. Magmatic lineage and petrogenetic implications. *Journal of Asian Earth Science* **38**, 147–61.

Mahapatro, S. N., Tripathy, A. K., Nanda, J. K. & Rath, S. C. 2013. Petrology of the Udayagiri Anorthosite Complex, Eastern Ghats Belt, India. *Journal of the Geological Society of India* **82**, 319–29.

Maji, A., Bhattacharya, A. & Raith, M. 1997. The Turkel anorthosite complex revisited. *Proceedings of the Indian Academy of Science* **106**, 313–25.

Maji, A. K. & Sarkar, S. S. 2004. Quantitative genetic modelling of the Turkel anorthosite, Eastern Ghats Mobile Belts, India. *Journal of Asian Earth Science* **24**, 199–211.

Majka, J., Be'eri-Shlevin, Y., Gee, D. G., Ladenberger, A., Claesson, S., Konečný, P. & Klonowska, I. 2012. Multiple monazite growth in the Åreskutan migmatite: evidence for a polymetamorphic Late Ordovician to Late Silurian evolution in the Seve Nappe Complex of west-central Jämtland, Sweden. *Journal of Geosciences* **57**, 13–23.

McDonough, W. F. & Sun, S.-S. 1995. The composition of the Earth. *Chemical Geology* **120**, 223–53.

Mezger, K. & Cosca, M. A. 1999. The thermal history of the Eastern Ghats belt (India), as revealed by U–Pb and $^{40}Ar$–$^{39}Ar$ dating of metamorphic and magmatic minerals: implications for the SWEAT correlation. *Precambrian Research* **94**, 251–71.

Montel, J. M., Foret, S., Veschambre, M., Nicollet, C. & Provost, A. 1996. Electron microprobe dating of monazite. *Chemical Geology* **131**, 37–53.

Mukherjee, A. B., Bhattacharya, A. & Chakravorty, S. C. 1986. Convergent phase equilibria at the anorthosite-granulite interface near Bolangir, Orissa, India and thermal evolution of a part of the Indian shield. *Precambrian Research* **3**, 69–104.

Mukherjee, A. B., Jana, P. & Das, S. 1999. The Banpur-Balugaon and Bolangir Anorthosite Diapirs of the Eastern Ghats, India: implications for the Massif Anorthosite Problem. *International Geology Review* **4**, 206–42.

Nanda, J. K. & Panda, P. K. 1999. Anorthosite–leuconorite–norite complex from Jugasaipatna, Kalahandi district, Eastern Ghats Belt of Orissa sector. *Gondwana Research Group Memoir* **5**, 89–104.

NASIPURI, P. & BHATTACHARYA, A. 2007. Melt-assisted interior to margin switch from dislocation to diffusion creep in coarse grained plagioclase: evidence from a deformed anorthosite pluton. *Journal of Structural Geology* **29**, 1327–38.

NASIPURI, P., BHATTACHARYA, A. & SATYANARAYANAN, M. 2011. Localized pluton deformation and linked focused flow of low-volume fraction residual melt in deforming plagioclase cumulates. *Geological Society of America Bulletin* **123**, 669–80.

NASIPURI, P. & BHADRA, S. 2013. Structural framework for the emplacement of the Bolangir anorthosite massif in the Eastern Ghats Granulite Belt, India: implications for post-Rodinia pre-Gondwana tectonics. *Mineralogy and Petrology* **107**, 861–80.

PARRISH, R. R. 1990. U–Pb dating of monazite and its application to geological problems. *Canadian Journal of Earth Sciences* **27**, 1431–50.

PAUL, D. K., BARMAN, T. R., MCNAUGHTON, N. J., FLETCHER, I. R., POTTS, P. J., RAMAKRISHNAN, M. & AUGUSTINE, A. F. 1990. Archean–Proterozoic evolution of Indian charnockites: isotopic and geochemical evidences from granulites of the Eastern Ghats belt. *Journal of Geology* **98**, 253–326.

PRABHAKAR, N. 2013. Resolving poly-metamorphic Paleoarchean ages by chemical dating of monazites using multi-spectrometer U, Th and Pb analyses and sub-counting methodology. *Chemical Geology* **347**, 255–70.

PRASAD, S., BHATTACHARYA, A., RAITH, M. M. & BHADRA, S. 2005. The origin of orthopyroxene/biotite + plagioclase coronas from the Bolangir anorthosite complex (India), and implications for reconstructing P-T paths. *American Mineralogist* **90**, 291–303.

RAITH, M., BHATTACHARYA, A. & HOERNES, D. 1997. A HFSE and REE enriched ferrodiorite suite from the Bolangir Anorthosite Complex, Eastern Ghats Belt. *Proceedings of the Indian Academy of Sciences – Earth and Planetary Sciences* **106**, 299–311.

RAITH, M. M., MAHAPATRO, S. N., UPADHYAY, D., BERNDT, J., MEZGER, K. & NANDA, J. K. 2014. Age and *P–T* evolution of the Neoproterozoic Turkel Anorthosite Complex, Eastern Ghats Province, India. *Precambrian Research* **254**, 87–113.

RAMAKRISHNAN, M., NANDA, J. K. & AUGUSTINE, P. F. 1998. Geological evolution of the Proterozoic Eastern Ghats Mobile Belt. *Geological Survey of India Special Publication* **44**, 1–21.

RASMUSSEN, B., FLETCHER, I. R. & SHEPPARD, S. 2005. Isotopic dating of the migration of a low grade metamorphic front during orogenesis. *Geology* **33**, 773–6.

RASMUSSEN, B. & MUHLING, J. R. 2007. Monazite begets monazite: evidence for dissolution of detrital monazite and reprecipitation of syntectonic monazite during low-grade regional metamorphism. *Contributions to Mineralogy and Petrology* **154**, 675–89.

REKHA, S., BHATTACHARYA, A. & VISWANATH, T. A. 2013. Microporosity linked fluid focusing and monazite instability in greenschist facies para-conglomerates, western India. *Geochimica et Cosmochimica Acta* **105**, 187–205.

RICKERS, K., MEZGER, K. & RAITH, M. M. 2001. Evolution of the continental crust in the Proterozoic Eastern Ghats Belt, India and new constraints for Rodinia reconstruction: implications from Sm–Nd, Rb–Sr and Pb–Pb isotopes. *Precambrian Research* **112**, 183–210.

SARKAR, A., BHANUMATHI, L. & BALASUBRAHMANYAN, M. N. 1981. Petrology, geochemistry, and geochronology of the Chilka Lake igneous complex, Orissa State, India. *Lithos* **14**, 93–111.

SCHANDL, E. S. & GORTON, M. P. 2004. A textural and geochemical guide to the identification of hydrothermal monazite; criteria for selection of samples for dating epigenetic hydrothermal ore deposits. *Economic Geology* **99**, 1027–35.

SCHÄRER, U., DE PARSEVAL, P., POLVE, M. & DE SAINT BLANQUAT, M. 1999. Formation of the Trimouns talc–chlorite deposits (Pyrenees) from persistent hydrothermal activity between 112 Ma and 97 Ma. *Terra Nova* **11**, 30–7.

SENGUPTA, P., DASGUPTA, S., BHATTACHARYA, P. K., FUKUOKA, M., CHAKRABORTI, S. & BHOWMIK, S. 1990. Petrotectonic imprints in the sapphirine granulites from Anantagiri, Eastern Ghats mobile belt, India. *Journal of Petrology* **31**, 971–96.

SHAW, R. K., ARIMA, M., KAGAMI, H., FANNING, C. M., SHIRAISHI, K. & MOTOYOSHI, Y. 1997. Proterozoic events in the Eastern Ghats Granulite Belt, India: evidence from Rb–Sr, Sm–Nd systematics and SHRIMP dating. *Journal of Geology* **105**, 645–56.

SPEAR, F. S., PYLE, J. M. & CHERNIAK, D. 2009. Limitations of chemical dating of monazite. *Chemical Geology* **266**, 218–30.

STEIGER, R. H. & JÄGER, E. 1977. Subcommission on geochronology: convention on the use of decay constants in geo- and cosmochronology. *Earth and Planetary Science Letters* **36**, 359–62.

STEPANOV, A., HERMAN, J., RUBATTO, D. & RAPP, R. P. 2012. Experimental study of monazite/melt partitioning with implications for the REE, Th and U geochemistry of crustal rocks. *Chemical Geology* **300–301**, 200–20.

SUZUKI, K. & ADACHI, M. 1991a. Precambrian provenance and Silurian metamorphism of the Tsubonosawa paragneiss in the South Kitakami terrane, Northeast Japan, revealed by the chemical Th–U–total Pb isochron ages of monazite, zircon and xenotime. *Geochemical Journal* **25**, 357–76.

SUZUKI, K. & ADACHI, M. 1991b. The chemical Th–U–total Pb isochron ages of zircon and monazite from the gray granite of the Hida Terrane, Japan. *Journal of Earth and Planetary Science* **38**, 11–38.

SUZUKI, K. & KATO, T. 2008. CHIME dating of monazite, xenotime, zircon and polycrase: protocol, pitfalls and chemical criterion of possibly discordant age data. *Gondwana Research* **14**, 569–86.

TAK, M. W. 1971. Some observations on the petromineralogical and chemical studies of the anorthositic rocks of the Bolangir-Patna district, Orissa. *Indian Minerals* **26**, 1–68.

TAK, M. W., MITRA, D. & CHATTERJEE, P. K. 1966. A note on the occurrence of anorthosite in the Bolangir-Patna District, Orissa. *Indian Minerals* **20**, 339–42.

TORSVIK, T. H. 2003. The Rodinia jigsaw puzzle. *Science* **300**, 1379–81.

TOWNSEND, K. J., MILLER, C. F., D'ANDREA, J. L., AYERS, J. C., HARRISON, T. M. & COATH, C. D. 2000. Low temperature replacement of monazite in the Ireteba granite, Southern Nevada: geochronological implications. *Chemical Geology* **172**, 95–112.

VEEVERS, J. J. 2007. Pan-Gondwanaland post-collisional extension marked by 650–500 Ma alkaline rocks and carbonatites and related detrital zircons: a review. *Earth Science Reviews* **83**, 1–47.

VEEVERS, J. J. & SAEED, A. 2009. Permian-Jurassic Mahanadi and Pranhitae-Godavari Rifts of Gondwana India: provenance from regional paleoslope and U–Pb/Hf analysis of detrital zircons. *Gondwana Research* **16**, 633–54.

Watson, E. B. & Harrison, M. 1983. Zircon saturation revisited: temperature and composition effects in a variety of crustal magma types. *Earth and Planetary Science Letters* **64**, 295–304.

Williams, M. L., Jercinovic, M. J., Goncalves, P. & Mahan, K. 2006. Format and philosophy for collecting, compiling, and reporting microprobe monazite ages. *Chemical Geology* **225**, 1–15.

Williams, M. L., Jercinovic, M. J. & Hetherington, C. J. 2007. Microprobe monazite geochronology: understanding geologic processes by integrating composition and chronology. *Annual Review of Earth and Planetary Sciences* **35**, 137–75.

Williams, M. L., Jercinovic, M. J. & Terry, M. P. 1999. Age mapping and dating of monazite on the electron microprobe: deconvoluting multistage tectonic histories. *Geology* **27**, 1023–6.

Xing, L., Trail, D. & Watson, E. B. 2009. Monazite/melt partition coefficients for U, Th: preliminary results from experiments. *American Geophysical Union (Fall Meeting abstract #V51A-1666)*.

Xing, L., Trail, D. & Watson, E. B. 2013. Th and U partitioning between monazite and felsic melt. *Chemical Geology* **358**, 46–53.

Zhu, X. K. & O’Nions, R. K. 1999*a*. Zonation of monazite in metamorphic rocks and its implications for high temperature thermochronology: a case study from the Lewisian terrain. *Earth and Planetary Science Letters* **171**, 209–20.

Zhu, X. K. & O’Nions, R. K. 1999*b*. Monazite chemical composition; some implications for monazite geochronology. *Contributions to Mineralogy and Petrology* **137**, 351–63.

Zhu, X. K., O’Nions, R. K., Belshaw, N. S. & Gibb, A. J. 1997. Significance of in situ SIMS chronometry of zoned monazite from the Lewisian Granites, northwest Scotland. *Chemical Geology* **135**, 35–53.